JGR Planets

RESEARCH ARTICLE
10.1029/2022JE007278

Special Section:
ExoMars Trace Gas Orbiter - One Martian Year of Science

Martian Atmospheric Temperature and Density Profiles During the First Year of NOMAD/TGO Solar Occultation Measurements

Miguel Angel López-Valverde[1], Bernd Funke[1], Adrian Brines[1], Aurèlien Stolzenbach[1], Ashimananda Modak[1], Brittany Hill[1], Francisco González-Galindo[1], Ian Thomas[2], Loic Trompet[2], Shohei Aoki[3], Gerónimo Villanueva[4], Giuliano Liuzzi[4,5], Justin Erwin[2], Udo Grabowski[6], Francois Forget[7], José Juan López-Moreno[1], Julio Rodriguez-Gómez[1], Bojan Ristic[2], Frank Daerden[2], Giancarlo Bellucci[8], Manish Patel[9], Ann-Carine Vandaele[3], and the NOMAD team

[1]Instituto de Astrofísica de Andalucia (IAA/CSIC), Granada, Spain, [2]Belgian Royal Institute for Space Aeronomy, Brussels, Belgium, [3]Japan Aerospace Exploration Agency (JAXA), Kashiwa, Japan, [4]NASA Goddard Space Flight Center, Greenbelt, MD, USA, [5]American University, Washington, DC, USA, [6]Karlsruhe Institute of Technology, Institute of Meteorology and Climate Research, Karlsruhe, Germany, [7]Laboratoire de Meteorologie Dynamique, Paris, France, [8]Institute for Space Astrophysics and Planetology, Rome, Italy, [9]Open University, Milton Keynes, UK

Key Points:

- Temperature and density profiles up to 90 km are retrieved from Nadir and Occultation for Mars Discovery (NOMAD) first year of solar occultations, covering two seasons of Mars Year 34
- NOMAD temperatures agree well with climate model predictions below 50 km but are wavier and globally colder by about 10 K at high altitudes
- We report large thermal tides producing warm layers at 80 km in the morning terminator. Also strong warming by the 2018 global dust storm

Correspondence to:
M. A. López-Valverde,
valverde@iaa.es

Citation:
López-Valverde, M. A., Funke, B., Brines, A., Stolzenbach, A., Modak, A., Hill, B., et al. (2023). Martian atmospheric temperature and density profiles during the first year of NOMAD/TGO solar occultation measurements. *Journal of Geophysical Research: Planets*, *128*, e2022JE007278. https://doi.org/10.1029/2022JE007278

Received 2 MAR 2022
Accepted 27 OCT 2022

Abstract We present vertical profiles of temperature and density from solar occultation (SO) observations by the "Nadir and Occultation for Mars Discovery" (NOMAD) spectrometer on board the Trace Gas Orbiter during its first operational year, which covered the second half of Mars Year 34. We used calibrated transmittance spectra in 380 scans, and apply an in-house pre-processing to clean data systematics. Temperature and CO_2 profiles up to about 90 km, with consistent hydrostatic adjustment, are obtained, after adapting an Earth-tested retrieval scheme to Mars conditions. Both pre-processing and retrieval are discussed to illustrate their performance and robustness. Our results reveal the large impact of the MY34 Global Dust Storm (GDS), which warmed the atmosphere at all altitudes. The large GDS aerosols opacity limited the sounding of tropospheric layers. The retrieved temperatures agree well with global climate models (GCM) at tropospheric altitudes, but NOMAD mesospheric temperatures are wavier and globally colder by 10 K in the perihelion season, particularly during the GDS and its decay phase. We observe a warm layer around 80 km during the Southern Spring, especially in the Northern Hemisphere morning terminator, associated to large thermal tides, significantly stronger than in the GCM. Cold mesospheric pockets, close to CO_2 condensation temperatures, are more frequently observed than in the GCM. NOMAD CO_2 densities show oscillations upon a seasonal trend that track well the latitudinal variations expected. Results uncertainties and suggestions to improve future data re-analysis are briefly discussed.

Plain Language Summary The detailed variation of temperature and density with altitude is of paramount importance to characterize the atmospheric state and to constrain the chemistry and dynamics as a whole. The Nadir and Occultation for Mars Discovery (NOMAD) instrument on board the Trace Gas Orbiter (TGO) has among its key targets the characterization of the thermal state with unprecedented vertical resolution. This is the target of this work, where we analyzed transmittance spectra obtained from the NOMAD solar occultation channel, with a state-of-the-art retrieval scheme, adapted from Earth to Mars conditions and geometry. We applied it to the first year of TGO observations, which covered the last two Mars seasons of Mars Year 34. The results permit to study the temperature structure up to 90 km and its seasonal and latitudinal variations, revealing the impact of the MY34 Global Dust Storm, a warm layer at mesospheric altitudes not present in climate models, more frequent cold pockets than in current global climate models, and generally, colder temperature at those altitudes, all of which can be of importance for the validation of these climate models.

1. Introduction

The Nadir and Occultation for Mars Discovery (NOMAD) and the Atmospheric Chemistry Suite (ACS) are the two key instruments on board the ExoMars 2016 Trace Gas Orbiter (TGO), primarily devoted to trace gas detection and mapping (Korablev et al., 2018; Vandaele et al., 2018). The solar occultation (SO) observational

strategy of these two instruments offer excellent opportunities to sound up to very high in the atmosphere in unprecedented vertical resolution in order to perform unique science at mesospheric and thermospheric altitudes (López-Valverde et al., 2018). The thermal structure of an atmosphere is of pivotal importance to understand its radiation, dynamics and chemistry, all of which in turn affect such state. An excellent review of past observations of the atmospheric thermal state in Mars can be found in Smith et al. (2017). The precise characterization of the atmospheric structure is necessary to correctly interpret the search for trace species, and is also in itself one of the goals of the TGO mission, and of NOMAD in particular. For this reason, NOMAD performs routine observations in several spectral intervals to achieve a good mapping of the atmospheric thermal state, and the analysis of these data is the primary goal of this work.

This work, together with other three companion manuscripts in this special issue, represent the first effort carried out in the Instituto de Astrofísica de Andalucía/Consejo Superior de Investigaciones Cientificas (IAA/CSIC) within our scientific plan for the exploitation of both NOMAD and ACS datasets with a common analysis and retrieval strategy. This consists of using an state-of-the-art retrieval scheme, described below, to both instruments. Here we report its application to NOMAD SO data, focused on the first year of the TGO science phase, from April 2018 to March 2019, which covers approximately two Mars seasons. These range from solar longitudes Ls 160° to Ls 360°, that is, the Southern spring and summer seasons, sometimes collectively names as the Martian perihelion period.

Following Smith et al. (2017), we will refer to the altitudes below about 50 km as troposphere or lower atmosphere and those above as mesosphere or middle atmosphere. We separate the mesosphere in lower and upper, as those regions below and above 90 km respectively, the upper one extending up to the mesopause, around 120 km (López-Valverde et al., 2018). This work is devoted to the study of one of the diffraction orders in the NOMAD/SO channel, with in-house label # 149, which approximately covers the spectral interval 3,349–3,375 cm^{-1}, and was used extensively in the NOMAD science team for the study of the thermal structure on Mars during its first year of operations. As we will show below, this SO order permits to sound up to 90 km altitude, that is, our target regions in this work are the troposphere and the lower mesosphere of Mars.

There are two recent publications presenting temperature profiles from TGO SO measurements by ACS. First, Fedorova et al. (2020) presented temperatures from the near-infrared (NIR) channel during the first year of TGO science phase, which matches well the seasonal period and the altitude range covered in this work. Second, Belyaev et al. (2021) presented profiles up to the mesopause, around 120 km, using a diffraction order containing H_2O spectral lines, in a work devoted to H_2O abundances at high altitudes. This second work presented temperatures in two consecutive perihelion seasons, for MY34 and MY35. The first one matches well the period studied here. We will make some comparisons with their results below.

The structure of the present work continues this Introduction with a Section 2 devoted to describe some relevant characteristics of the NOMAD/SO channel and the subset of measurements used in this work. Section 3 details the methodology and pipeline we used for these data analysis, pre-processing and inversion. Section 4 presents the 3-D distribution of temperatures and densities obtained, and describe them to gain insight into atmospheric variability. Comparisons with previous works and with global climate model simulations are also presented there. Finally, Section 5 presents a summary of the major results and plans to improve and extend this work to more NOMAD data, and also to ACS SO data.

In addition to this work, other two manuscripts studying the thermal structure in SO data from the TGO/NOMAD and ACS instruments have been submitted to this issue. In the first one, Trompet et al. (2023) analyzed the NOMAD/SO channel's diffraction order 148 during Mars Years 35 and 36, excluding MY34 and focusing on mesospheric altitudes. The second presents profiles up to thermospheric altitudes combining two diffraction orders of the ACS/MIR channel, in a study covering two full Martian years which is an extension of Belyaev et al. (2021). Each one of these works uses different inversion techniques and approximations, obtaining different retrieval errors and vertical resolutions. Our plan is to extend the present work to a larger data set in the near future in order to perform a proper comparison with those two investigations.

2. NOMAD/SO Measurements

2.1. NOMAD Instrument

The NOMAD spectrometer, in routine operations since April 2018 on board the ExoMars 2016 TGO, has 3 channels from the ultraviolet (UV) to the near-infrared (IR), each one with its own telescopic pointing and internal optics and detectors. NOMAD main scientific objectives include the search for trace species, the track of their sources and sinks, and the mapping of the thermal structure and the atmospheric composition at high sampling rate in the vertical, from the ground up to the thermosphere (López-Valverde et al., 2018; Vandaele et al., 2018). Its SO channel, in contrast to the other two channels, was designed for only SO measurements and covers the range between 2.3 and 4.3 μm (2,320–4,350 cm^{-1}) with a nominal resolving power close to 20,000 (Neefs et al., 2015). With a slit oriented quasi-perpendicular to the surface of the planet in the limb, the SO channel samples the atmosphere at one tangent altitude every second approximately. The SO detector's focal plane array is made up of 320 pixels along the spectral axis and 256 rows in the spatial direction, with 30 μm × 30 μm individual pixel sizes (Neefs et al., 2015). The SO slit is projected into 30 detector rows (a little larger than the Sun projected size) times 2 pixels wide. This represents a 1 × 12 km as projected onto the limb. Up to 6 diffraction orders of the echelle grating can be selected at a given altitude. From the downlink limitation that only 24 spectra can be transmitted to Earth per observation, this implies that only 4 spectra per order can be recorded (Vandaele et al., 2018). The usual SO operations combine pixels in the spatial dimension into four "detector bins," hence producing the required four spectra, each pointing to a slightly different tangent altitude. These detector bins, which can contain up to a maximum of six individual pixels, determine the instantaneous field-of-view (FOV), which is normally 2 × 4 arcmin, or about 1 × 2 km at the limb. Depending on the β-angle (that between the TGO orbital plane and the solar direction), the number of altitudes sampled per scan can be very variable, but at least a few dozen points in the vertical are usually available. Together with the mentioned FOV, the SO channel allows to build vertical profiles with unprecedented resolution in every scan, twice per orbit. This channel contains an Acousto-Optical Tunable Filter (AOTF) which selects different spectral windows (with a width that varies from 20 to 35 cm^{-1}). Routine operations are planned ahead of time with specific scientific goals in mind, that is, with one particular combination of diffraction orders in each scan. More details on the original design, calibration and expected performance, and regular operations can be found in several publications (Liuzzi et al., 2018; Robert et al., 2016; Thomas et al., 2016; Trompet et al., 2016; Vandaele et al., 2018, 2019).

2.2. Data Set

NOMAD science operations began in April 2018, once the TGO spacecraft reached its final quasi-circular orbit, at about 400 km above the Martian surface, after a long aerobraking phase and a commissioning phase. In this work we selected data during the first year of routine operations in its science phase, from April 2018 until March 2019, which approximately covers the second half of MY34: solar longitudes L_s = 160°–355°. For the retrievals of temperature and density in this work we selected diffraction order 149 (3,349–3,375 cm^{-1}) which was very frequently used during this first year of observations and contains CO_2 ro-vibrational lines of intermediate strength (see Figure 1). As we show below in Section 4, this order permits a good sounding at tangent altitudes up to about 90 km. During the period selected, we used about 380 type-A scans (internal name for scans using that diffraction order at all altitudes during the SO scan), spanning a diverse set of latitudes and solar longitudes, typical of the particular SO mapping by TGO, as shown in Figure 1. There are stronger CO_2 ro-vibrational bands within the SO range than those mapped by diffraction order 149, in particular those in the 2.7 μm region, dominated by the two fundamental bands of the major CO_2 isotope. These are captured by SO orders 159–165 and are intended to sound up to thermospheric altitudes due to their much larger optical thickness. We studied them in detail but found them to be very sensitive to error correlations at high altitudes and to the strong non-linear dependence of their absorption on temperature around the mesopause. We plan to tackle these bands in a near future after a better handling of the noise correlation and after a combination of adjacent orders; both of these extensions are within our ongoing improvements in the SO data analysis.

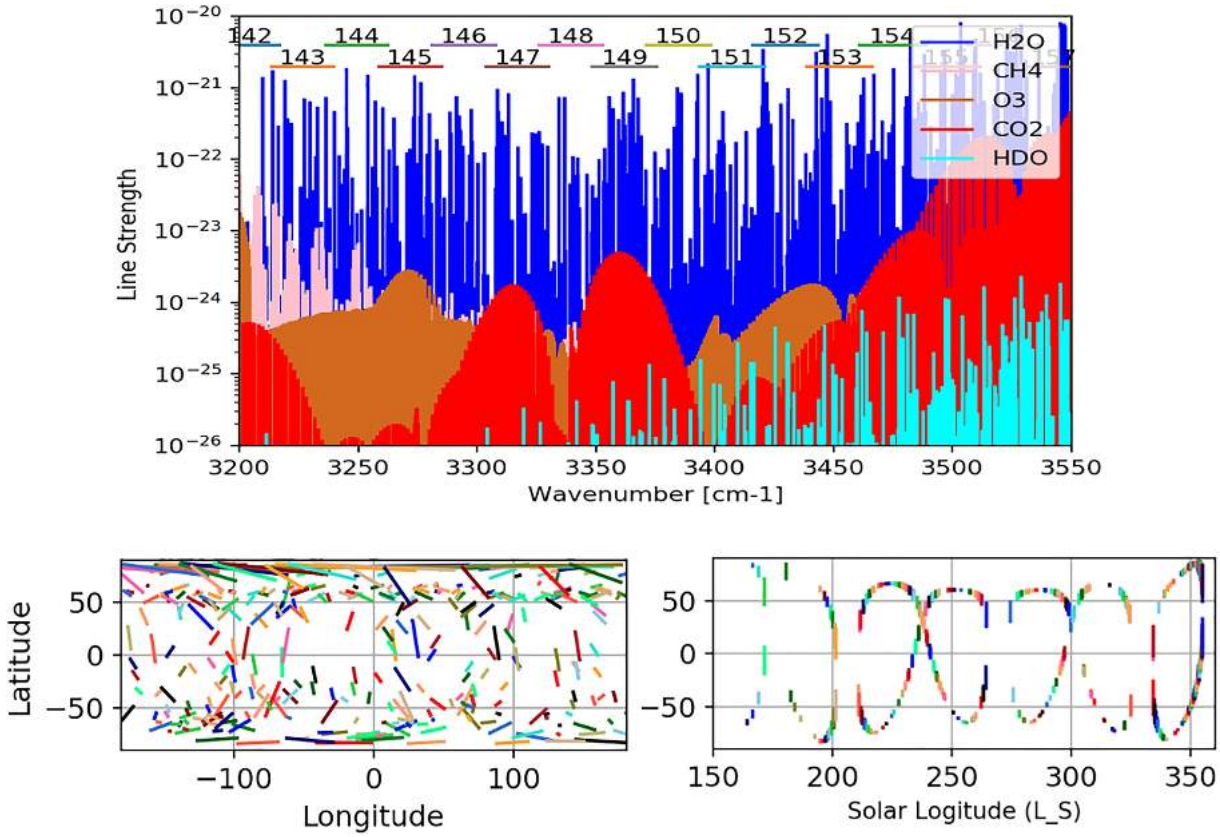

Figure 1. Top panel: Spectral location of Nadir and Occultation for Mars Discovery (NOMAD)/solar occultation diffraction order 149, and other adjacent orders, with indication of the strongest ro-vibrational absorption lines by some atmospheric species (positions and line strengths from Hitran2016). Bottom panels: latitude, longitude and solar longitude of the about 350 scans with solar occultation measurements in order 149 during the first year of NOMAD operations. Colors in the bottom panels are arbitrary, used for clarity.

3. Data Analysis

The NOMAD/SO data used in this work are Level 1A calibrated transmittance from the latest pipeline processing at the Belgian Institute for Space Aeronomy (IASB-BIRA, NOMAD's PI team) (Thomas et al., 2021). The inversion of temperature and density presented here is part of a broader effort at IAA/CSIC devoted to the scientific exploitation of NOMAD and ACS measurements with a common data analysis scheme. We followed a sequential retrieval strategy, starting with the inversion of atmospheric opacity from the continuum in the SO data, then the temperature and density, and these are used later in the inversion of trace species (see the two companion papers on H_2O and CO by Brines et al. (2023) and by Modak et al. (2023), respectively). At the core of the inversion scheme is a line-by-line radiative transfer Forward Model (KOPRA, see e.g., Stiller (2000)) and an inversion control program (or Retrieval Control Program (RCP) in short, see von Clarmann et al. (2003)) originally developed at the University of Karlsruhe, and briefly described below in Section 3.2. The calibrated transmittances are not yet suitable to be ingested by the retrieval suite but a very important cleaning or pre-processing is needed first. This is described next in some detail, as it affects no only this work but also the companion retrieval works.

3.1. Data Cleaning and Pre-Processing

The pre-processing phase of the data analysis at IAA is schematically shown in Figure 2 and is devoted to correct for remaining imprecisions still present in the calibrated transmittances. These features include spectral shifts and residual spectral bending across the diffraction orders which can be quite significant in some spectra. These problems are common to all diffraction orders but different for each one of them and variable from scan to scan, as they depend on temperature effects on the detector, on TGO orbital conditions which in turn impact the space

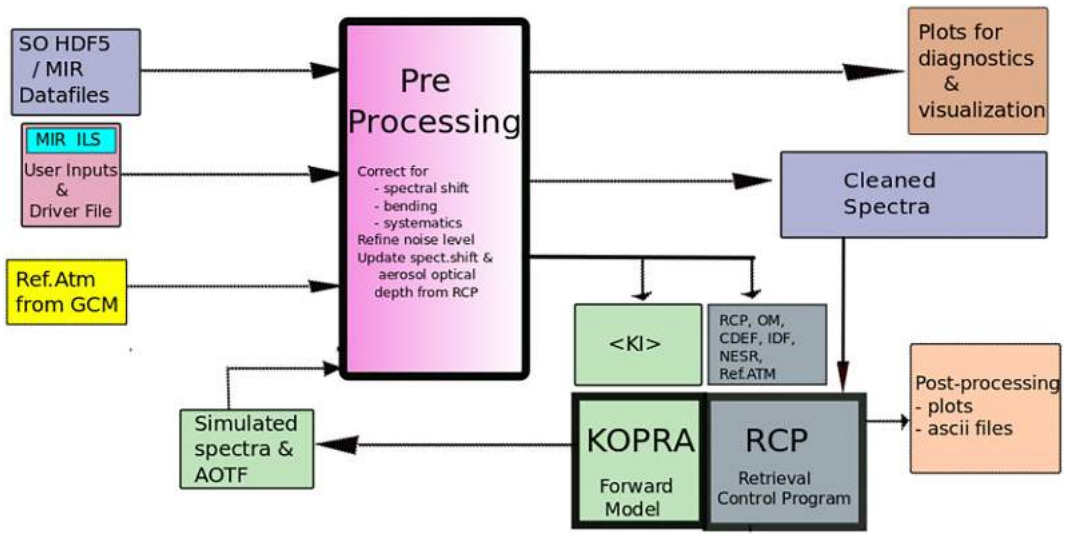

Figure 2. Pipeline of the Nadir and Occultation for Mars Discovery and Atmospheric Chemistry Suite data analysis at IAA. The preprocessing block performs cleaning of residual spectral shifts and bendings, characterization of the ILS from the observed spectra, in addition to auxiliary plots and splitting of the spectra in spectral micro-windows before the inversion, this second step being performed by KOPRA and RCP. See text for details.

signals, and on drifts through time in the behavior of the grating's blaze response (Liuzzi et al., 2018; Thomas et al., 2021). These effects are shown for one specific scan in Figure 3.

Other effects, like the precise response of the AOTF and the NOMAD/SO line shape (ILS) also require analysis at this pre-processing level, as well as during the inversion of scientific data. Our effort devoted to the AOTF and ILS characterization aligns with parallel efforts by other teams in the NOMAD consortium and are described in a companion paper by Villanueva et al. (2022) in this special issue. In brief, we are using an asymmetric sync-squared function for the AOTF whose center accounts for variations in detector temperature, and a double-Gaussian ILS with separation and ratio between the Gaussians which vary across each order and changing through the different SO diffraction orders.

An important defect in the spectra is the bending, which is very variable and can be very significant. It is particularly worrying for the precise determination of the actual atmospheric opacity. Fortunately its spectral shape can approximately be characterized (and corrected) by a simple polynominal fitting. However this correction is only approximate if the gas absorption lines are not taken into account. A more careful treatment is needed, especially for exploiting spectra at high tangent altitudes, where the absorption lines are weak and a simple bending correction of the full order can alter the baseline continuum and produce large biases.

Our pre-processing strategy essentially splits the measured transmittance in contributions along the ray path starting at the Sun and going through the atmosphere, first, and through the SO channel optics later. One of the possible characterizations of these contributions can be expressed as:

$$T_m = T_{GAS} \times T_{AEROSOLS} \times T_b \times R1_{NOISE}$$

where T_m is the measured transmittance, T_{GAS} is the atmospheric transmittance due to the target species (CO_2 in the case of temperature and density retrievals), and $T_{AEROSOLS}$ is the absorption of the solar flux produced by the atmospheric aerosols along the Line of Sight (LOS), which is considered here as a contaminant component and is computed by the pre-processing from the continuum component in the spectra. The term T_b stands for the residual bending, to be computed and corrected for. Finally, the term $R1_{NOISE}$ stands for a random Gaussian centered at 1 and with a standard deviation similar to the noise transmittance. For the correction we simply minimize the ratios $1 - T_m/T_{SIMUL}$, where we have combined into the term, T_{SIMUL}, the observed aerosol slant transmittances together with a large set of line-by-line forward model calculations carried out with KOPRA for the expected atmospheric state (extracted from a global climate model, as explained below). To avoid unstable results when the atmospheric plus aerosol transmittances are very low (at low tangent altitudes), the actual function to minimize is modified

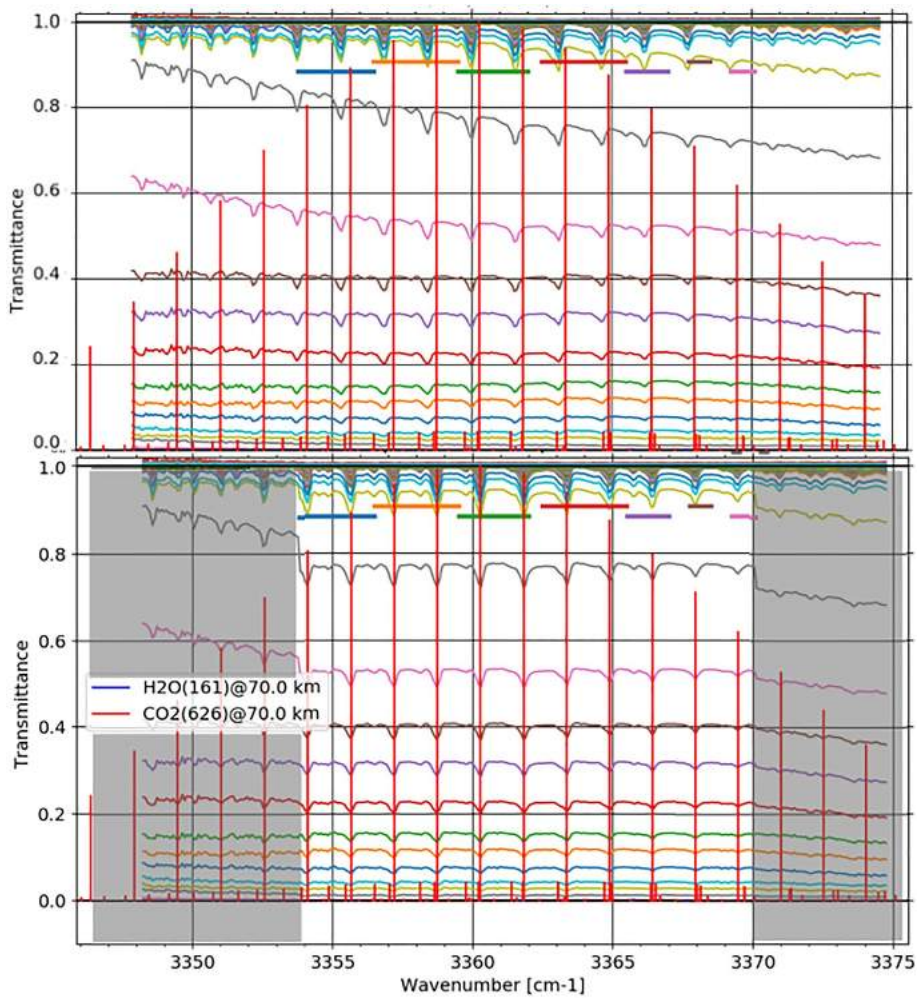

Figure 3. Example of our cleaning method applied to diffraction order 149 in one specific scan (20180423_204351_1p0a_SO_A_I). Top panel, all the original spectra (calibrated transmittances) taken in this scan, showing clear bending effects and spectral shifts. Bottom panel, spectra after cleaning. Notice the cleaning is only applied to a subset of the full diffraction order (the rest is shaded in gray in the bottom panel). Vertical red solid lines indicate the expected position of the CO_2 spectral lines (Hitran2016). The seven short horizontal lines in different colors near the top of the panels indicate the micro-windows used in this order (see text for details).

to $1 - (1 + T_m)/(1 + T_{SIMUL})$. This is applied to each tangent altitude in every scan. We found this method very robust and precise, using synthetic data, although it is time consuming due to the brute-force calculation required to generate all the T_{SIMUL}.

Once the bending is corrected, the residual spectral shifts across the order are computed and corrected, again from comparisons with the line-by-line simulations at each spectrum (or tangent altitude) during a scan. For practical reasons and in preparation for the retrievals, we perform this cleaning in a set of spectral micro-windows. As found by other teams, the residual spectral shift in a scan is usually at the level of 0.1–0.3 cm^{-1}, and is not constant through the diffraction order but usually follows a linear variation, as shown in Figure 3. However, this shift is approximately constant with altitude, as far as the data are not very noisy or strongly contaminated by aerosol absorption. These conditions need to be taken into account to define the "meaningful" altitude range for a correct shift correction. Then each order in each scan is corrected in that altitude range, and the same correction is applied at all other altitudes.

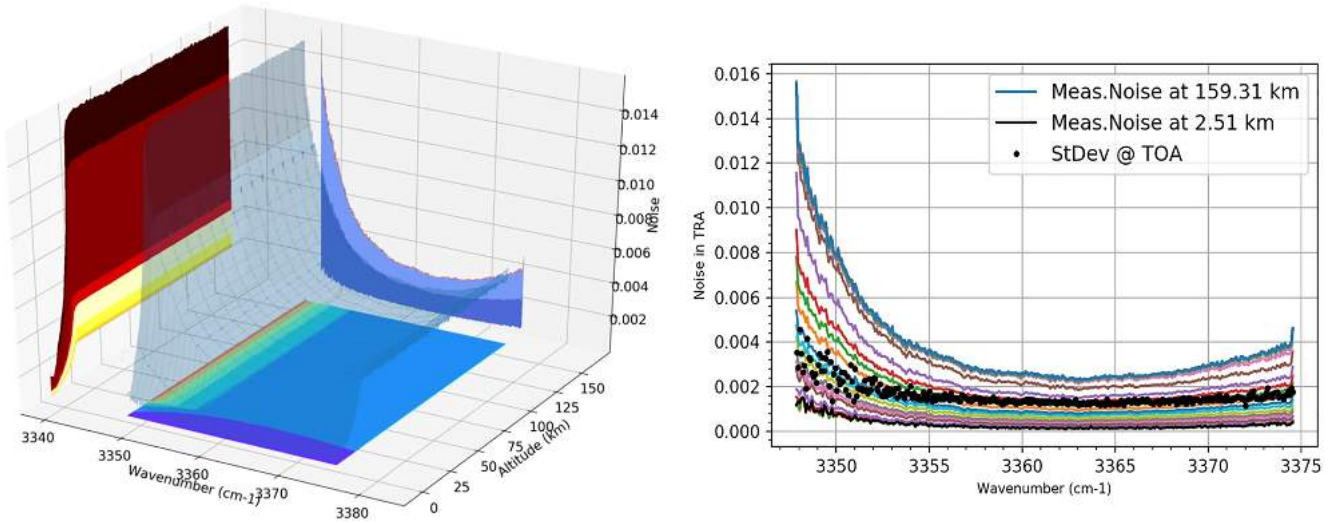

Figure 4. Measurement noise in transmittance in the order 149 of scan *20180423_204351_1p0a_SO_A_I*, typical of all scans in this diffraction order. Left panel, variations in the spectral and altitude dimensions. Right-hand panel: alternative view of the projection onto the wavenumber-noise plane to appreciate better the quasi-random variations; each line represents a noise spectrum (at one tangent altitude). The black-dots are the standard deviation of transmittance vertical profiles near the top of the atmosphere. The color scales in both panels are arbitrary. See text for details.

3.2. Retrieval Scheme

In Figure 2, RCP stands for Retrieval Control Program, and is a multi-parameter non-linear least squares fitting of measured and modeled spectra (von Clarmann et al., 2003). At the core of this processor is a state-of-the-art line-by-line radiative forward model named KOPRA (Karlsruhe Optimized Radiative transfer Algorithm) described by Stiller (2000). Very well tested on Earth atmosphere remote sounding projects, Kopra integrates the RT equation along the observed LOS which is computed for an ellipsoidal planetary surface including consideration of refraction. KOPRA was recently adapted to limb emissions on Mars (Jiménez-Monferrer et al., 2021), and now it has been adapted to SO data on Mars for the first time, and in particular to the NOMAD/SO channel with implementation of the asymmetric AOTF transfer function and the double Gaussian ILS.

Key inputs to RCP are the initial guess and a priori information of the quantities to be retrieved, as well as the NOMAD data, after the cleaning described above. The a priori temperature and density profiles are taken from a specific run of the Mars Global Climate Model developed at the Laboratoire de Météorologie Dynamique (LMD-MGCM) (Forget et al., 1999, 2009), using the recent implementations of the water cycles (Navarro et al., 2014) and the dust scenarios appropriate for MY34 (Montabone et al., 2015, 2020). For each NOMAD/SO scan, a temperature and density profile was extracted from the model at the location (latitude, longitude) and time (local time and Ls) of a central point in the occultation (for a tangent altitude of 50 km).

RCP solves iteratively the inverse problem (Rodgers, 2000) until convergence is achieved. The calculation of the model spectra and Jacobians is performed with KOPRA, being called in each step of the iteration. For the temperature inversion, we perform a hydrostatic adjustment in each iteration, to account for the varying atmospheric state when the thermal structure is changed, and therefore to guarantee realistic results in the temperature/pressure structure. This hydrostatic adjustment assumes a reference pressure at the lowermost tangent altitude available, and that pressure value is taken from the a priori reference atmosphere. As we detail below, these tangent altitude and reference pressure are dependent on the aerosol loading along the LOS.

Convergence is reached when the change of retrieval parameters with respect to the previous iteration produces improvements in the difference measured—simulated spectra until they are smaller than the measurement noise. The SO noise plays a central role in the inversion and deserves some explanation. The measurement covariance matrix is calculated from the noise-equivalent spectral radiance provided with the NOMAD level 1a calibrated data. Figure 4 shows the NOMAD measurement noise in one particular scan, typical of the calibration in this order 149. The noise function shown in the left-hand panel is projected into three planes for easier visualization. The projection on the wavenumber-noise plane is also shown in the right-hand panel as an alternative view, using

arbitrary colors at each altitude. The noise transmittances in this right-hand panel show more clearly their strong spectral variations with increases toward the edge of the diffraction orders, where the sensitivity is lower due to the shape of the AOTF. They are also clear the variations with altitude, following the dependence on shot noise, that is, on the solar flux received in the detector (Thomas et al., 2016). This variation is specially strong at tropospheric altitudes, when the solar radiation is strongly absorbed, either by gas species or by dust. An analysis of the vertical oscillations in the transmittances at high altitudes gives smaller values than these "nominal" ones. Such a calculation is shown with black dots in the right-hand panel of Figure 4. Comparing with the higher envelope, which is the measurement noise at high tangent altitudes, our estimate is lower by a factor 2, and this is very representative of most scans. This means that the actual random component in the nominal noise is smaller. This result is specific of order 149, and in all our temperature retrievals we reduced the nominal measurement error by such a factor 2.

We use a Tikhonov-type regularization optimized for each diffraction order. This is dependent on the measurement noise and was optimized, first by performing synthetic retrievals, and later by examination of a large set of actual retrievals. The value used in this work, common to all scans, varies with altitude, as the measurement noise and the line absorption changes with tangent altitude across each scan, and was selected as a compromise between error propagation and vertical resolution.

At the end of the inversion, temperatures, densities and also an adjustment of the atmospheric pressure is obtained. This last retrieval product, internally called "Line-Of-Sight in the altitude," was originally intended to account for possible biases in satellite pointing. In our case this represents deviations from the nominal altitude registration which improve the best fit. For the radiative tranfer calculations the atmosphere is divided into 1-km wide layers from the surface up to 60 km, 2.0 km width layers from 60 to 90 km, 2.5 km-wide layers at 90 to 130 and 5 km wide layers above. The output retrieved vectors also share this grid, which is common to all the IAA retrievals using NOMAD data and presented in this special issue.

Outside the SO measurement altitude range, we impose a strong regularization constraint, to give a large weight to the a priori information (to its vertical gradient, which will be imposed on the data). For the CO_2 density, a strong diagonalization at all altitudes below 80 km is used, for stability reasons, which effectively assumes the volume mixing ratio (VMR) in the a priori value is correct. It is well known that the CO_2 VMR is close to one up to the homopause, surely above the altitude range studied here. However, the CO_2 absolute density will be variable and determined from the NOMAD data via the hydrostatic inversion mentioned above, consistently with the thermal structure.

At low altitudes we avoid large dust contamination by filtering observations where the aerosol opacity is greater than a given value. For order 149 we use a maximum slant opacity of 2.0. Also we avoid steep gradients in the aerosol slant opacity, larger than 0.08 km^{-1}.

The instrument transfer function of an AOTF (nominally a sinc-square) leads to the mixing of different echelle diffraction orders into the central one. Details of this effect in the case of NOMAD have been discussed previously (Liuzzi et al., 2018; Mahieux et al., 2015; Thomas et al., 2021). Following these guidelines and our own tests, we are accounting for the flux contribution of ±4 adjacent orders around the 149 (i.e., orders 145–153). Contributions beyond these orders are very small, well below 5%. However, the contribution from orders 148 and 150 are significant (between 10% and 30% at some wavelengths) and we found that the fitting of these other orders' absorption lines is normally difficult, even after a careful fine tuning of the AOTF for this specific order. A practical solution adopted in this work is to use a powerful feature in RCP, namely, the use of internal spectral micro-windows instead of the full spectral range of the diffraction order. With the use of micro-windows we can select portions of the spectrum which are particularly valuable in terms of information content, and at the same time, omit very contaminated spectral segments. After extensive experimentation we adopted a set of 7 micro-windows for order 149, of diverse spectral widths, mostly located in the central part of the order to avoid the noisier edges, and which contain some of the strongest CO_2 lines in the order. They are shown with color horizontal bars in Figure 3. The pre-processing/cleaning is focused on the central part of the diffraction order, the region covered by the microwindows; this is why we obscured the outer spectral regions in Figure 3.

Figures 5 and 7 show the performance of the temperature inversion in one specific scan, *20180620_0240338_1p0a_SO_A_I*, obtained on 20 June 2018, for Ls 196° and at 55° N latitude, where a heavy dust loading was found below about 20 km. The Averaging Kernels in Figure 5 show a lack of information in this order above 95 km.

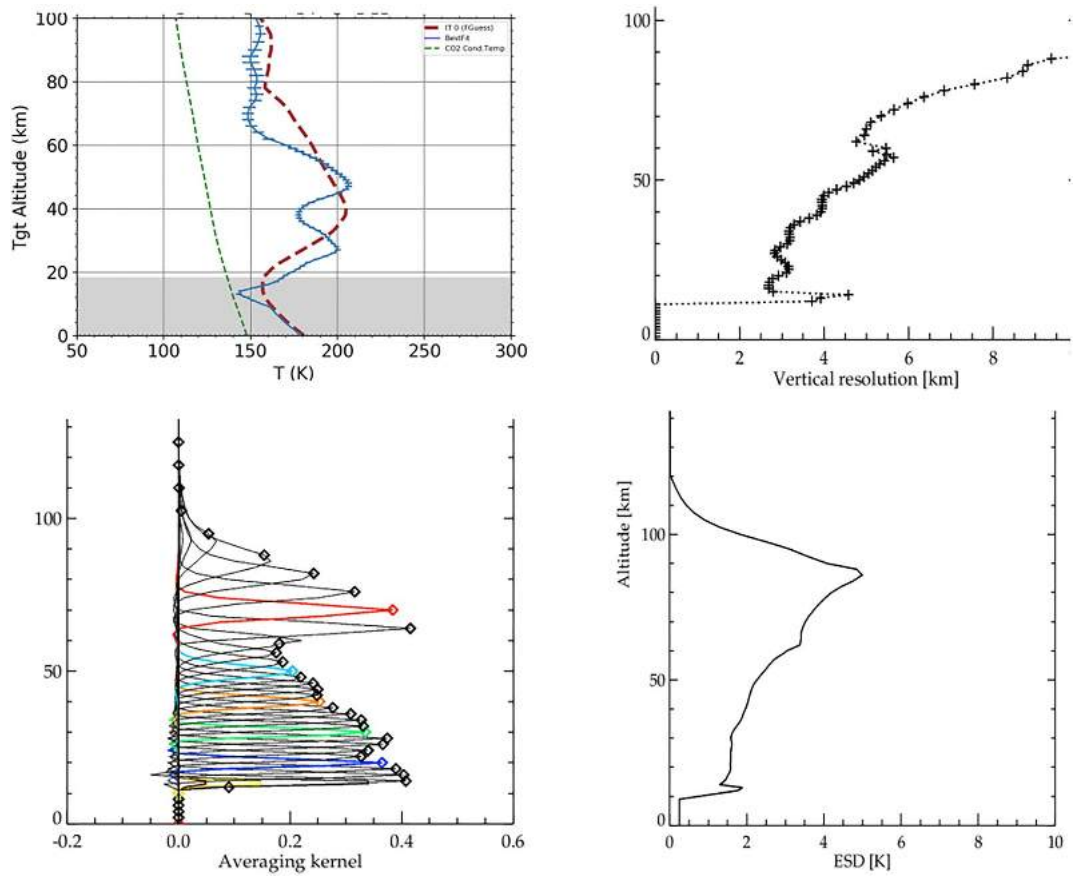

Figure 5. Retrieved temperature profile from scan *20180423_204351_1p0a_SO_A_I* with error bars (top-left panel), where the red dashed line is the a priori profile, and the green dashed line is the CO_2 condensation temperature, added for reference. Bottom-left: rows of the Averaging Kernel matrix selected at some altitudes. Bottom-right: retrieval error in the Temperature profile. Top-right: Vertical resolution, as given by the widths of the averaging kernel rows.

Averaging Kernels matrices are very useful as diagnostics of the performance of the retrieval, and are standard outputs of our inversion code RCP. For example, inspection of this matrix's rows illustrate the vertical resolution while its columns quantify the response to changes in the true state vector. Also the trace of this matrix gives the independent pieces of information, that is, the degrees of freedom, which in the case of the scan in Figure 5 is 19. For its calculation RCP makes use of Jacobians computed/updated in every time step of the inversion, taking into account all the spectral information present in the selected microwindows. Figure 5 shows that the retrieval errors usually increase with altitude, in this scan from about 2 K at 20 km to about 5 K around 90 km. The vertical resolution, given by the width of the Averaging Kernel rows, also vary significantly with tangent altitude, between 3 km in the lowermost tangent altitude up to 10 km at the top range in this scan. The best-fit spectra at the end of the inversion usually reproduces the NOMAD data very well. Figure 7 shows the best fit obtained for this scan at about 65 km altitude, where the retrieved temperature significantly differs from the a priori. Sometimes high altitude spectra go slightly above Transmittance = 1; these defects in the data are accounted for during the inversion by a simultaneous retrieval of the continuum at each altitude, which also includes a small shift in the continuum, as required for matching the data. To illustrate the robustness of the inversion against changes in the a priori, we show in Figure 6 the temperature inversion of another scan, *20180423_204351_1p0a_SO_A_I*, obtained at 65° S latitude and Ls 164°, arbitrary selected among the data set. We performed two retrievals, one using the nominal a priori GCM atmosphere and the other with an a priori profile arbitrary increased by 30 K at all altitudes. As shown in Figure 6, the retrieved temperature is basically the same in both runs up to 80 km; above this altitude the relatively large measurement noise decreases the information content and starts pulling the retrieved profile toward the assumed climatology.

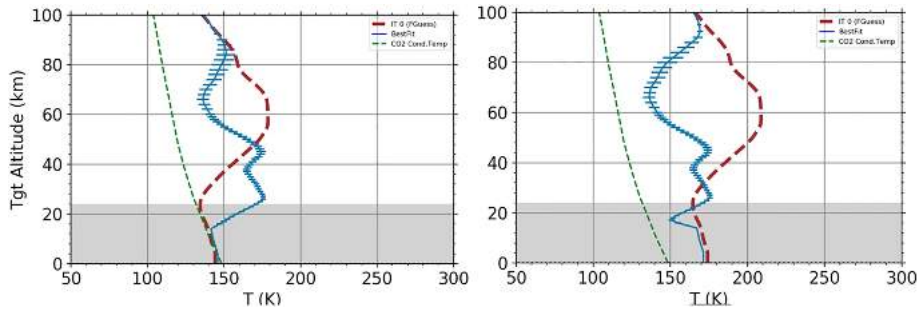

Figure 6. Effect of the a priori temperature on the retrieval for scan *20180423_204351_1p0a_SO_A_I*. Left panel: inversion using the nominal a priori temperature profile. Right panel: using the a priori increased by 30 K.

4. Results and Discussion

The retrieval strategy discussed above was applied to our selection of 380 NOMAD/SO scans observed during MY34, as mentioned above. The convergence rate was high, with a final 338 retrieved temperature and CO_2 density profiles. We describe and discuss here the main results obtained.

We only show here results with a significant amount of information directly derived from the data. In the lowermost tangent altitudes and above about 95 km we apply a condition on the diagonal of the Averaging Kernels, to filter values only above 0.03. Lower values are considered as too biased toward a priori/climatological values, due to very low depth of the absorption lines at high altitudes and to aerosol contamination at low tangent altitudes.

4.1. Global Envelope of Atmospheric Temperatures

Figure 8 shows all the temperature profiles retrieved in this work, put together in a single panel, with a similar plot for the LMD GCM profiles (our a priori). The dashed lines in blue and orange represent the envelope of all possible temperatures anywhere and anytime on Mars, taken from Smith et al. (2017), who compiled data from instruments Mars Climate Sounder and Thermal Emission Spectrometer, as well as from the Mars Climate Database simulations for extreme conditions.

The range of temperatures observed by NOMAD are quite similar to the GCM, although generally colder in the mesosphere. The global difference between 0.01 and 0.001 mb pressure levels (about 60–80 km altitude) seems to be over 10 K. In addition, and although possibly difficult to see in this Figure, the NOMAD temperatures seem to be wavier than in the GCM, and in particular we obtained excursions to very low temperatures at altitudes above 0.001 mb. At these altitudes, NOMAD temperatures reach values very close to the CO_2 condensation temperature, much closer that in the GCM.

4.2. Global Distribution of Temperatures

Figure 9 shows the global distribution of all the temperatures obtained, split in two hemispheres for clarity, and covering the second part of MY34. Some gaps in the maps correspond to lack of SO data as the TGO-Sun β-angle becomes too large. Given the peculiar TGO solar acquisition sequence, the latitudes and seasons are linked and this needs to be taken into account when inspecting the maps.

The vertical thermal structure generally presents what can be considered as a typical Martian pattern in the vertical, with the usual two broad thermal layers, a warmer troposphere and a colder mesosphere, except near polar regions where the thermal regime can be quite different (Smith et al., 2017). This follows the warming at low altitudes by convection from the surface and the local heating by solar absorption by airborne dust. On the other hand, the atmospheric radiative cooling to space by diverse CO_2 ro-vibrational bands becomes an important term of the energy budget as we move upwards to the mesosphere, where these bands become optically thinner. There is a significant variability upon this generic profile, depending on diverse parameters (surface temperatures and dust amounts, together with other energy budget terms including dynamics), all of which vary along the TGO track, as latitude and seasons change across the *X*-axis in Figure 9.

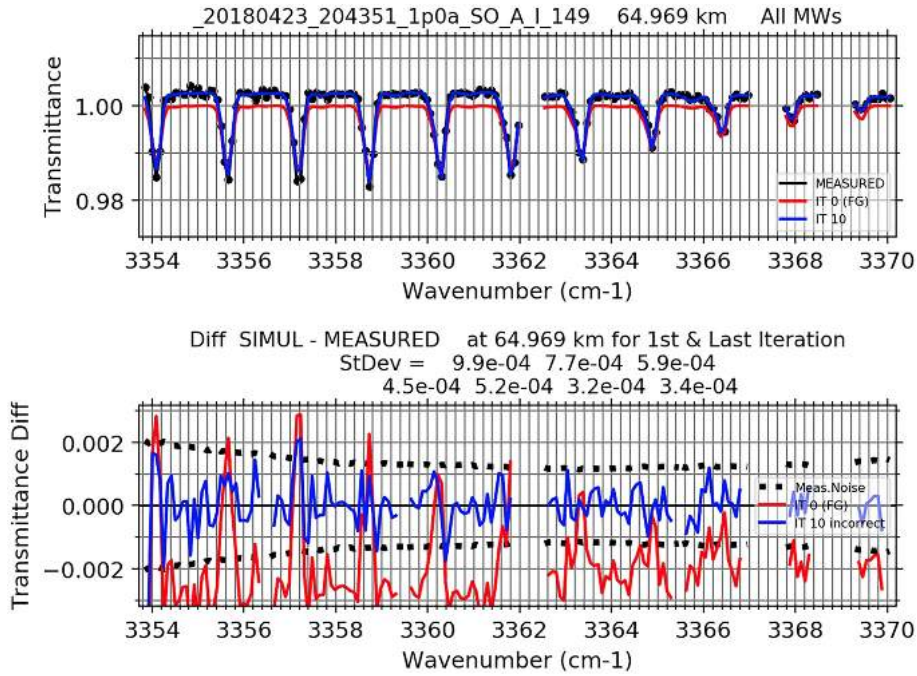

Figure 7. Best fit spectrum to the Nadir and Occultation for Mars Discovery (NOMAD) cleaned transmittances from scan *20180423_204351_1p0a_SO_A_I* at a tangent altitude of about 65 km. The top panel shows the measured spectrum in solid black line with dots, the best fit spectrum at the end of the inversion in blue, and the spectrum obtained with the a priori atmospheric profile in red. The spectrum is split in 7 segments which correspond to the 7 micro-windows used in the inversion (see text). The lower panel shows the residuals (Model fit—NOMAD) in blue, together with the same magnitude but with the model spectrum for the a priori atmosphere, in red. The dotted lines represent the NOMAD/SO measurement error used in the inversion.

4.3. MY34 Global Dust Storm

Several interesting features are observed in Figure 9, and the most prominent one is the strong warming period between Ls 190° and 220,° at all altitudes and in both hemispheres. This corresponds to the onset of the MY34 Global Dust Storm (GDS), which peaked around Ls 195°–205° (Montabone et al., 2020). As it is well known, the absorption of solar radiation by the dust particles, especially as they reach high altitudes, can be very efficient (Wolff et al., 2017). In this period the slant aerosol opacity is so large that the limb sounding using molecular spectral lines in this spectral region is impossible at tangent altitudes below 40 km, or even 55 km in some scans. We observe warm temperatures around 180 K up to 80–90 km altitude in the peak of the GDS, and tropospheric temperatures above 200 K up to 50 km.

The decay of the GDS seems apparent in Figure 9 by the progressive cooling at mesospheric altitudes from Ls 220°–240° in the Northern Hemisphere (NH) at mid latitudes. This is more difficult to see in the Southern Hemisphere (SH) as this period follows large changes in TGO latitude coverage as well. In fact, there seem to be several warming periods at mesospheric altitudes in the SH, around Ls 220°, 260°, 285°, 315°, and 340°, which coincide with the mapping of high latitudes in the SH. This seems to show a latitudinal gradient with warmer mesospheric temperatures at high latitudes during the whole perihelion season.

4.4. Global Distribution of Atmospheric Density

Similarly to Figure 9, Figure 10 shows the global distribution of all the CO_2 densities obtained. The strong exponential decrease in density with altitude seems to minimize other variations, with lower amplitudes, even using a log scale. Hence, in order to highlight these, we selected an altitude of 70 km and plotted in the two lower panels its variability with time, together with the GCM variability at that altitude. There are clear variations associated with the latitudinal change at the tangent point. For example, the three largest excursions in density, at Ls 355° in the NH and at Ls 170° and Ls 200° in the SH, are clearly associated to sudden changes in latitude in a short Ls

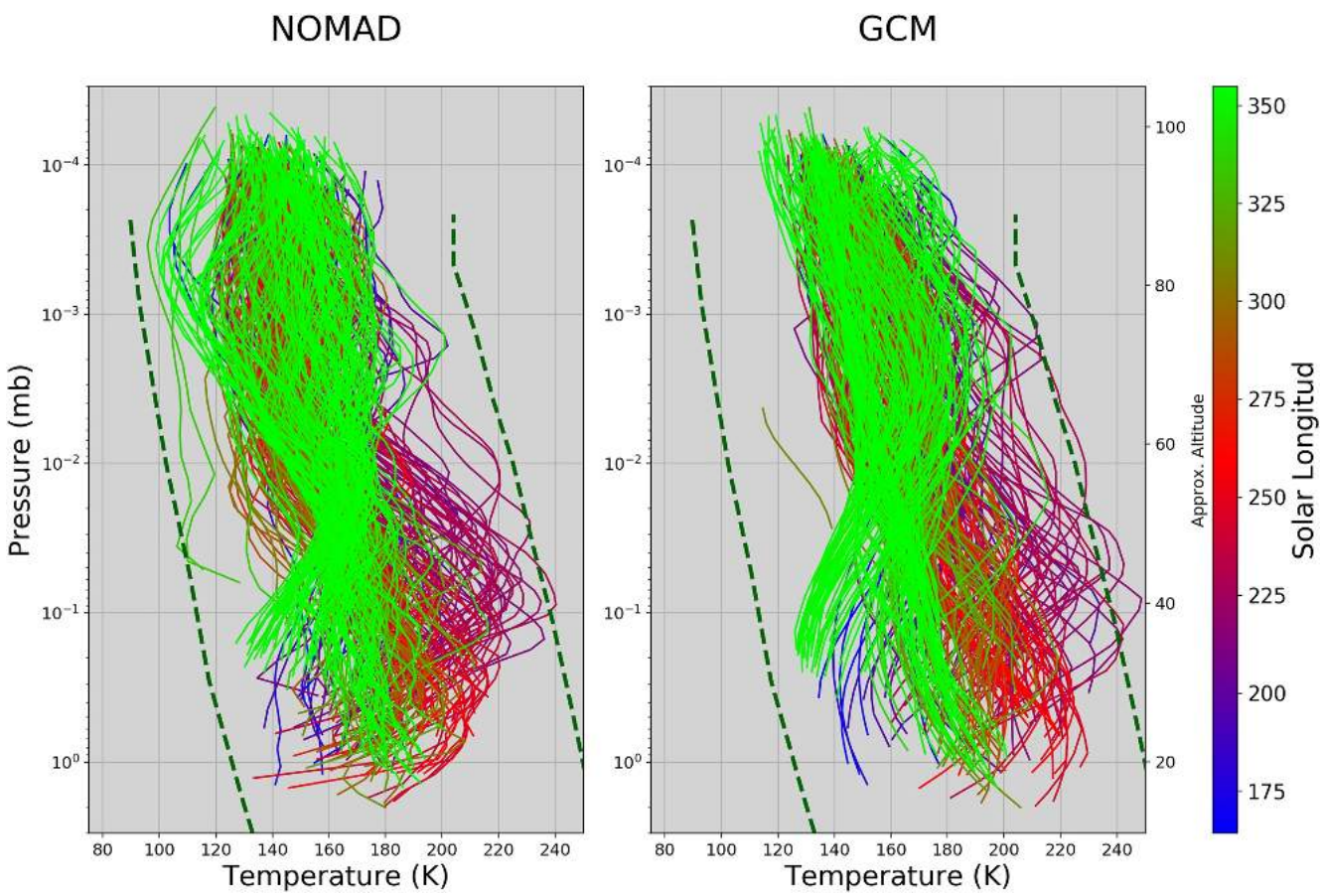

Figure 8. Envelope of all the retrieved temperature profiles (left-hand panel) compared to the a priori data, from the Laboratoire de Météorologie Dynamique (right-hand panel). The colors in each scan indicate the Solar Longitude. The thick dashed lines represent the extreme temperatures at any time and place on Mars, after Smith et al. (2017). Approximate altitudes added as a quick guide.

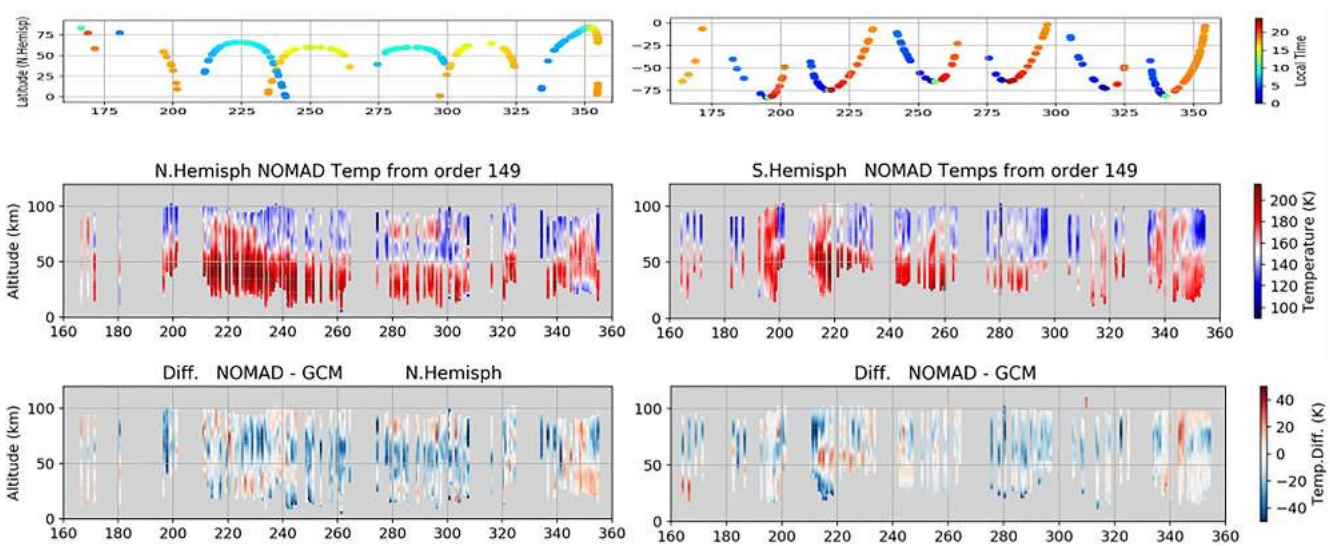

Figure 9. Distribution of all the retrieved temperatures with latitude and solar time throughout Mars Year 34, split in the two hemispheres (Northern Hemisphere in the left hand side panels and Southern Hemisphere in the right hand side panels). The two top panels show the latitudes and the Local Solar Time of the observations. The center panels show the temperatures, and the two lowermost panels the difference between the Nadir and Occultation for Mars Discovery retrievals and the global climate models (a priori).

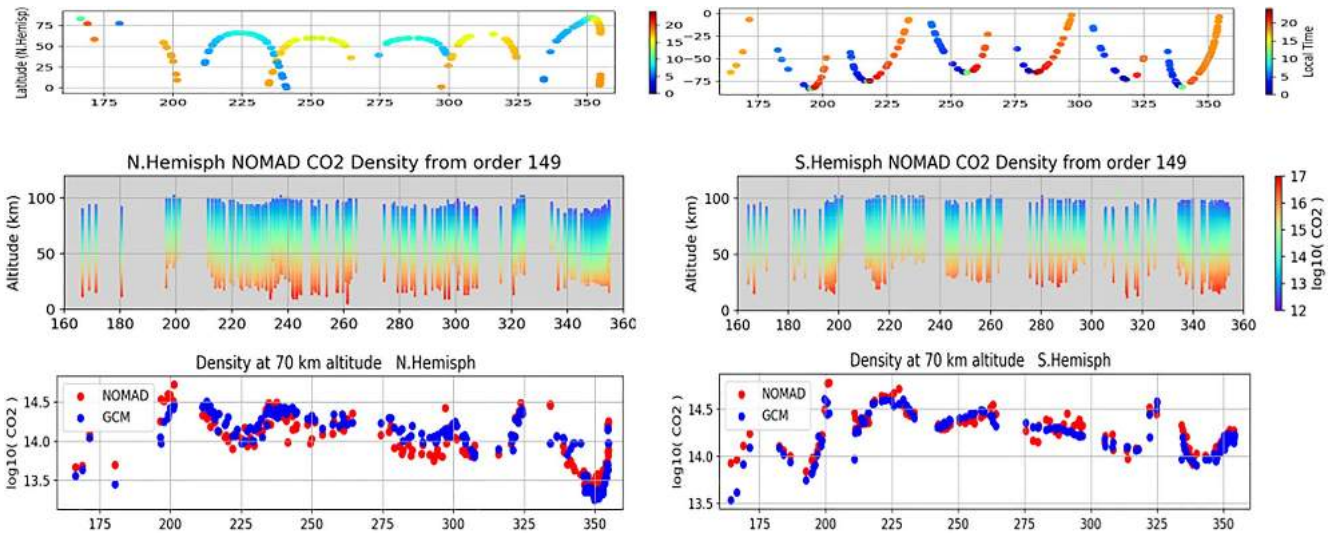

Figure 10. Global distribution of the retrieved CO_2 densities for Mars Year 34, split in the two hemispheres (Northern Hemisphere in panels on the left and Southern Hemisphere on the right). The top panels show the latitudes and the Local Solar Time of the observations and the central panels show the densities in log scale. The bottom panels show the density variation at 70 km altitude through the mission, including latitudinal and seasonal variations (see text); red dots: Nadir and Occultation for Mars Discovery densities, blue dots: global climate models data.

period. In both hemispheres the sign of the response is similar: as the orbit approaches lower latitudes the density increases, following the warmer troposphere at low latitudes. Averaging over these variations one would expect to discern a seasonal trend with a maximum around the summer in the SH, around Ls 270°, when the atmospheric density in Mars presents a maximum (Smith et al., 2017). However, in Figure 10 the maximum is observed around Ls 200°, as a response to the MY34 GDS.

This analysis is complementary and agrees with a similar analysis by Trompet et al. (2023) in a companion paper in this special issue, who studied the variation of the atmospheric density in NOMAD retrievals for MY35. In the absence of GDS, the MY35 presents a maximum around Ls 270° in their work. Also the absolute values of the densities at 70 km agree well between both retrieval teams.

4.5. Corrections for the Reference Pressure

During the temperature and density retrieval, our inversion processor finds whether a change in the line-of-sight pointing, or in other words, in the tangent altitudes, would produce a better model-data fit than with the nominal pointing. Usually the correction found is small but without this correction the temperature profiles would be incorrectly positioned. The variation, expressed in km at the tangent point, is shown in Figure 11. Some profiles should be moved up and some down, with a globally averaged negative value around 2 km. Figure 11 also shows the absolute value of this correction.

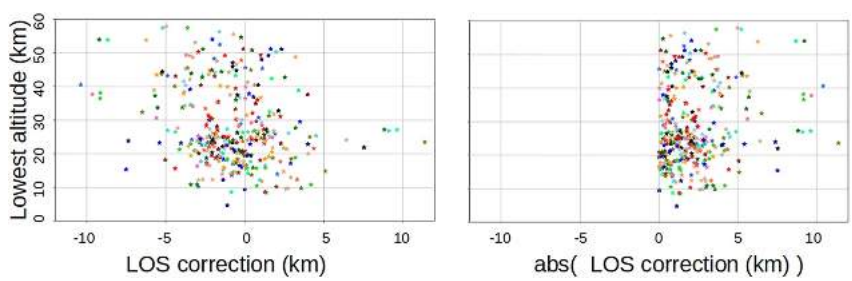

Figure 11. Distribution of the retrieved Line of Sight correction with altitude of all the retrieved profiles (left panel) and the same but in absolute values (right panel). See text for details.

The interpretation of this result is related to the assumed pressure reference for the hydrostatic adjustment. Pressure values from the GCM are taken at a given altitude, and a hydrostatic atmosphere is built with this assumption. The results shown in Figure 11 inform us that such an altitude seems to be wrong by a few km, according to NOMAD data. The envelope of the data points in the right-hand panel in this figure shows lower values at lower altitudes. This is suggesting that the pressure-altitude relationship is more correct in the GCM the lower we look in the atmosphere. This is not surprising, as the atmospheric variability should create differences with the GCM climatological state which increase with altitude.

4.6. Latitudinal Variations

During MY34 there are two seasonal periods, around Ls 180° and Ls 290°, where the TGO mapping covers a wide range of latitudes in a short Ls interval. These offer a good opportunity to observe and characterize the latitudinal variations in temperature. We have grouped the scans in these periods exactly in boxes Ls = 160°–190° and 285°–305° and show them in Figure 12, where they are compared to the same sampling and boxing in the GCM data (our a priori). Unfortunately, the numerous gaps in the data make it difficult to do a fine comparison on a pure altitude/latitude cross section map, but still some interesting results are clearly present.

For example, the NOMAD data in Ls Box #1 (left panels) seem to show a warm layer around 50 km around latitudes 60°N and 60°S, which is also seen in the GCM model and at similar altitudes. This agrees with the expected global description of the atmospheric temperatures in equinox conditions (seen in the bottom panels of Figure 12), in spite of the difference data-model (NOMAD temperature being generally colder than GCM at mesospheric altitudes). These warm layer is not seen in Ls Box #2 (right panels).

Another result which agree with the GCM simulations is the warm layer at the bottom of the observed altitudes in Ls Box #2 (right panels). These layers seem to correspond to the warming at high latitudes of the SH, typical of the Southern Summer solstice. These warm layers are absent in both model and data in the Ls Box #1 (left panels).

The latitudinal variations in the NOMAD temperatures seem to agree in these two periods with typical equinox and solstice conditions as simulated by the LMD-GCM.

4.7. Local Time Variations

Inspection of the orbit in Figure 1 or Figure 8 reveals a couple of periods with a significant variation in local time in a short Ls period and small variations in latitude as well. These two periods are analyzed here in the search for possible variations with local time. Period "CT Box1" covers latitudes 20°–50° in the NH during the bracket Ls 230°–250°, and period "CT Box2" covers latitudes 30°N–60°N and Ls 290°–310°. We grouped all the scans inside these boxes splitting them by their local time only, and are shown in Figure 13. The figure also shows the LMD GCM profiles for the same scans.

In CT Box1 there are no significant differences between the morning and evening results, neither in the NOMAD data nor in the model, although the NOMAD data shows a colder layer at 60 km altitude within a more wavy vertical profile. CT Box2 shows also a more wavy profile in NOMAD than in the model, with a possibly upward propagating wave with large amplitudes, around 30 K in the mesosphere, which is much weaker in the GCM. This oscillation seems to be smaller in the NOMAD evening profiles, although there are not many profiles to examine and one of them also presents a large oscillation. The warm layer at 80 km in the NOMAD morning data could be related to the recent finding of a warm layer at precisely that altitude at nighttime in stellar occultation data from IUVS/Maven (Nakagawa et al., 2020).

A similar warm layer was reported also by Belyaev et al. (2021) using ACS SO data in the ACS/MIR channel. The data used by Belyaev et al. (2021) are not exactly collocated with NOMAD observations. In their retrievals the warm layer was found as more localized around Ls 270°, and present in both MY34 and MY35 but only in the NH. Although not discussed by them, their results combined with ours indicate a peculiar period of time around perihelion, at the end of the Southern summer where thermal tides at mid latitudes seem to present very strong amplitudes, greatly affecting the lower mesosphere. It will be interesting to extend the current study to cover more Martian years, and also to compare more quantitatively with ACS/MIR results, in order to confirm this strong

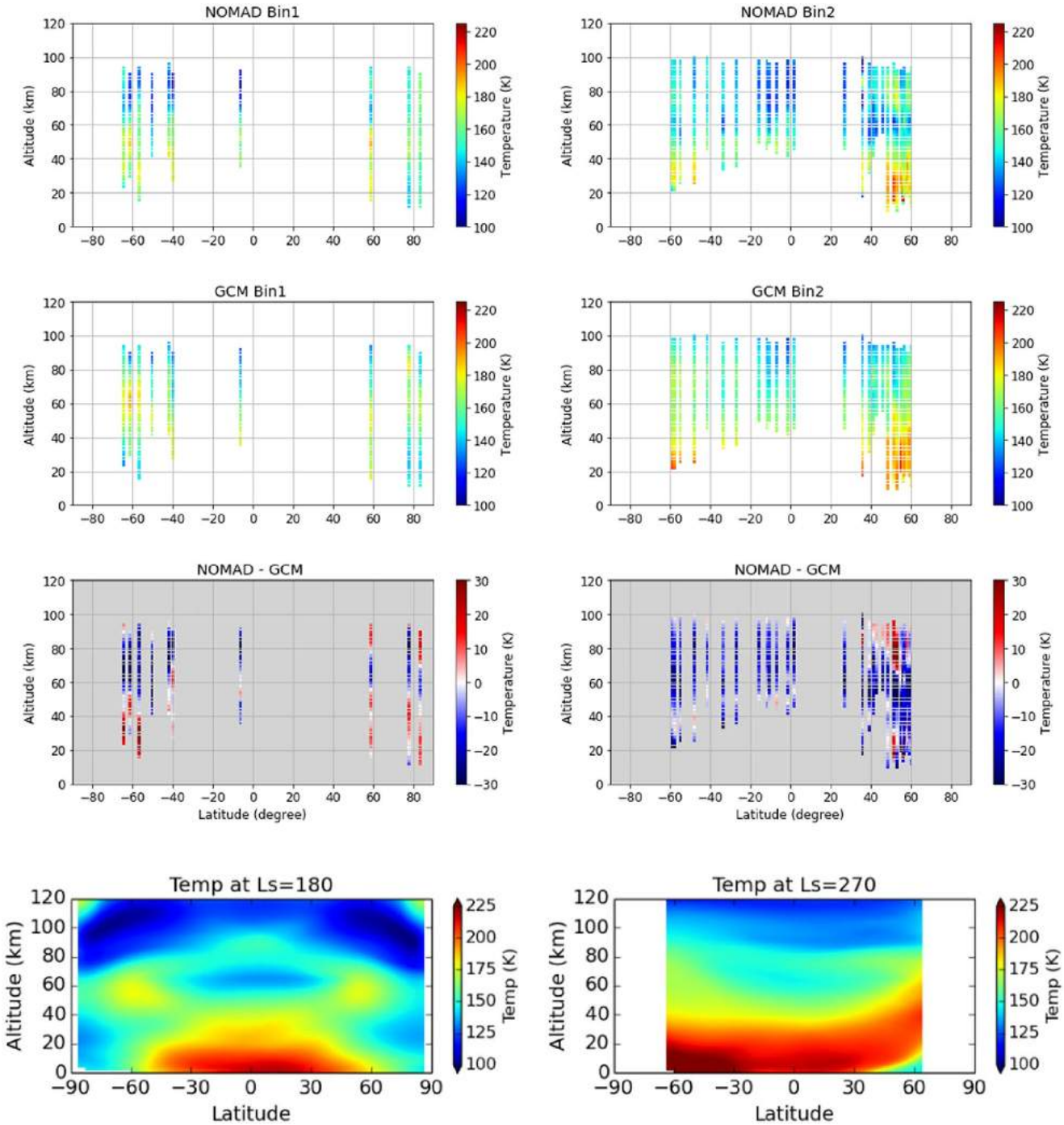

Figure 12. Latitudinal distribution of the retrieved Nadir and Occultation for Mars Discovery (NOMAD) temperatures in two seasonal periods. Left panels: period Ls = 160°–190°; right-hand side: period Ls = 285°–305°. Top panels: NOMAD retrieved temperatures; second from top: global climate models (GCM) temperatures at the same locations and local times; third panels from top: difference NOMAD-GCM; and bottom panels: altitude/latitude cross sections of the Laboratoire de Météorologie Dynamique temperatures at Ls 180° and 270°, for comparison.

thermal tide and to analyze its year-to-year variability with the good vertical resolution of these two instruments on board TGO.

Upward propagation of waves has been recently studied by Starichenko et al. (2021) but this work was very focused on gravity waves and small scale structures observed in the ACS/MIR temperature vertical profiles, not on the thermal tides.

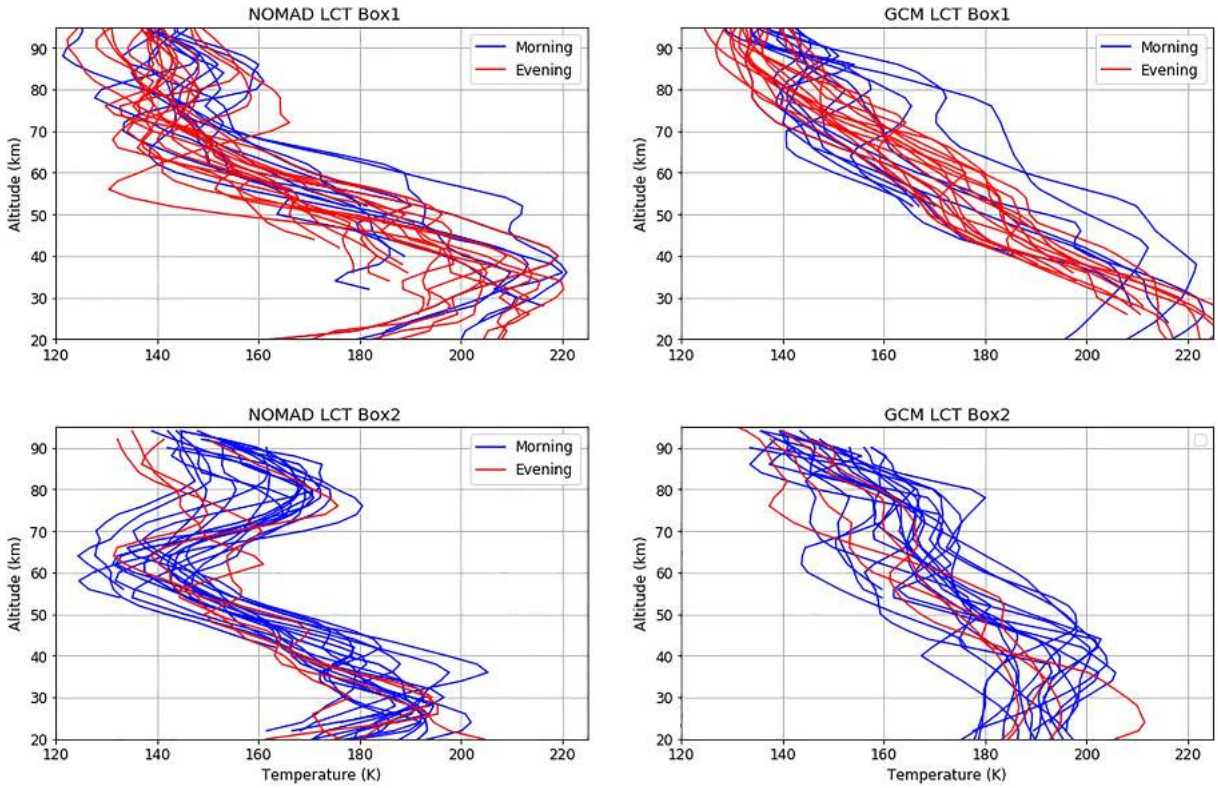

Figure 13. Local Time variations in 2 specific periods and locations, selected to minimize latitudinal and seasonal effects. Top panels: CT Box 1, defined by Latitudes 20°N–50°N and Ls 230°–250°. Bottom panels: CT Box 2, defined by Latitudes 30°N–60°N and Ls 290°–310°. See text for details.

4.8. Latitudinal-Seasonal Slices at Fixed Altitudes

Figure 14 shows the structure of the NOMAD temperatures in latitude - solar longitude cross sections at three altitudes, 30, 50, and 80 km, compared with the a priori GCM temperatures. Again we observe a NOMAD thermal field colder than the GCM at mesospheric altitudes and a better agreement in the troposphere. In this figure, and in spite of variability and differences, we observe that the 3-D map of NOMAD temperatures globally agree with the global thermal distribution simulated by the GCM for MY34. We observe a warm troposphere at 30 km at all latitudes during the GDS with a gradual cooling with time, in both data and model (left panels). At 50 km the warm layers are located at mid latitudes in both model and data but NOMAD does not see the warm branch at 60°N that the model simulated for the rest of MY34. It will be interesting to explore these comparisons in other Mars Years.

4.9. Comparison With ACS/NIR Temperatures

Temperature profiles from ACS/NIR have been reported by Fedorova et al. (2020) for a period of time similar to that covered in this work. Although a proper comparison campaign is beyond the scope of this manuscript, we have performed a first comparative study of a few dozens of profiles. We first looked for close coincidences to each of our NOMAD/SO retrieved profiles, defined as being observed by ACS/NIR on the same day, as determined by the solar longitude L_S, and within a small bracket in latitude, longitude and local time: $\Delta LAT < 3°$, $\Delta LON < 20°$ and $\Delta LCT = 0.5$ hr. Only six coincidences were found, and they are shown in Figure 15. The agreement between both instruments is quite good, and in four of the six profiles the differences are approximately within their error brackets. The altitude range sampled by both instruments is very similar in all the profiles. At the top of the altitude range, at and above 90 km, the ACS/NIR retrieval errors increase a lot and also in our NOMAD/SO data the a priori effect starts to be significant. At the bottom of the profiles, both retrievals are limited by the aerosol absorption along the LOS, in approximately the same manner. Some of the features observed in the thermal profiles indicate that the vertical resolution in both instruments is also similar.

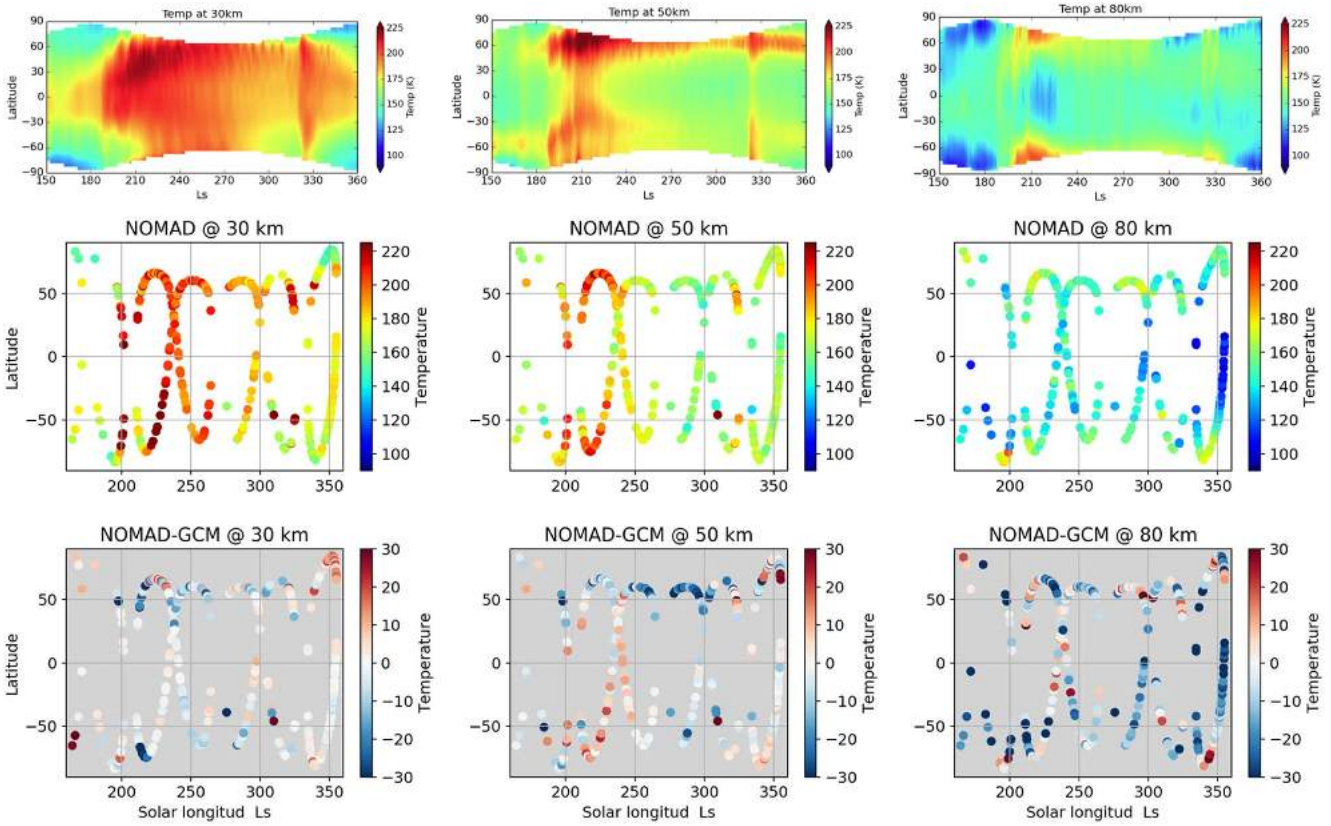

Figure 14. Temperature latitude-solar longitude cross sections at 3 different altitudes, 30 km (left panels), 50 km (central column's panels) and 80 km (right-hand panels). The retrieved temperatures are shown in the central row, while Latitude-Ls cross sections from the Laboratoire de M´et´eorologie Dynamique are shown in the top panel, for reference. See text for details.

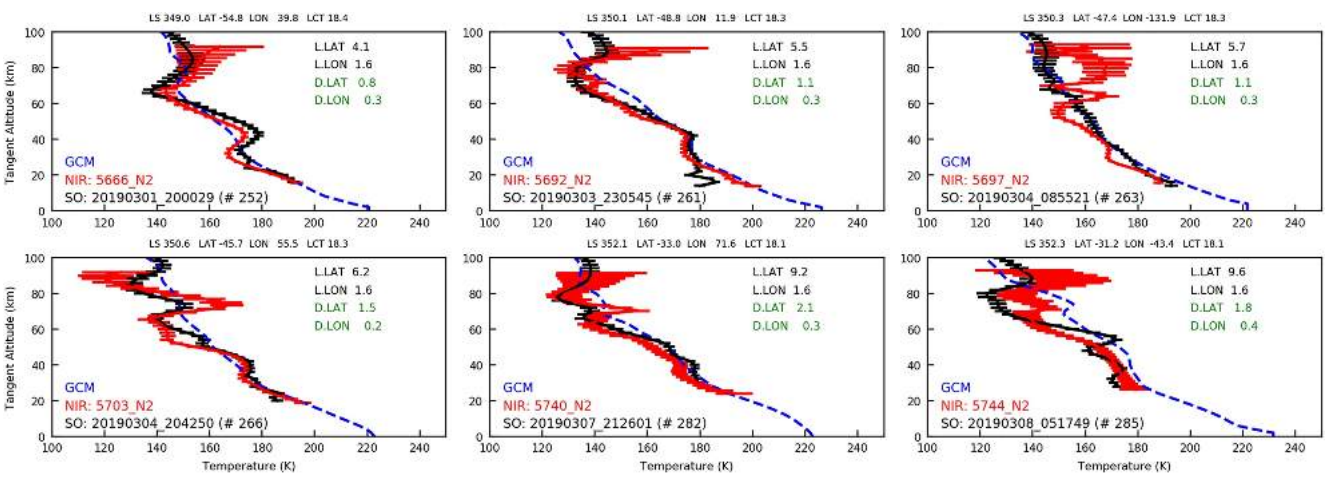

Figure 15. Comparison between Nadir and Occultation for Mars Discovery/solar occultation (NOMAD/SO) and ACS/NIR temperature profiles in the 6 closest coincidences, each of them in a separate panel. The panels titles indicate the locations of the profiles in latitude, longitude, local time and solar longitude. The NOMAD/SO temperature profile and error bars are in black, the ACS/NIR in red, and the global climate models a priori in blue. Each instrument's orbit number identifier is also included for easy reference; in the case of NOMAD/SO we also added a number in bracket for internal reference. L.LAT and L.LON indicate the extension of the NOMAD/SO profile in latitude and longitude (in degree), respectively. D.LAT and D.LON indicate the separation between the NOMAD/SO and ACS/NIR profiles in latitude and longitude respectively. See text for details.

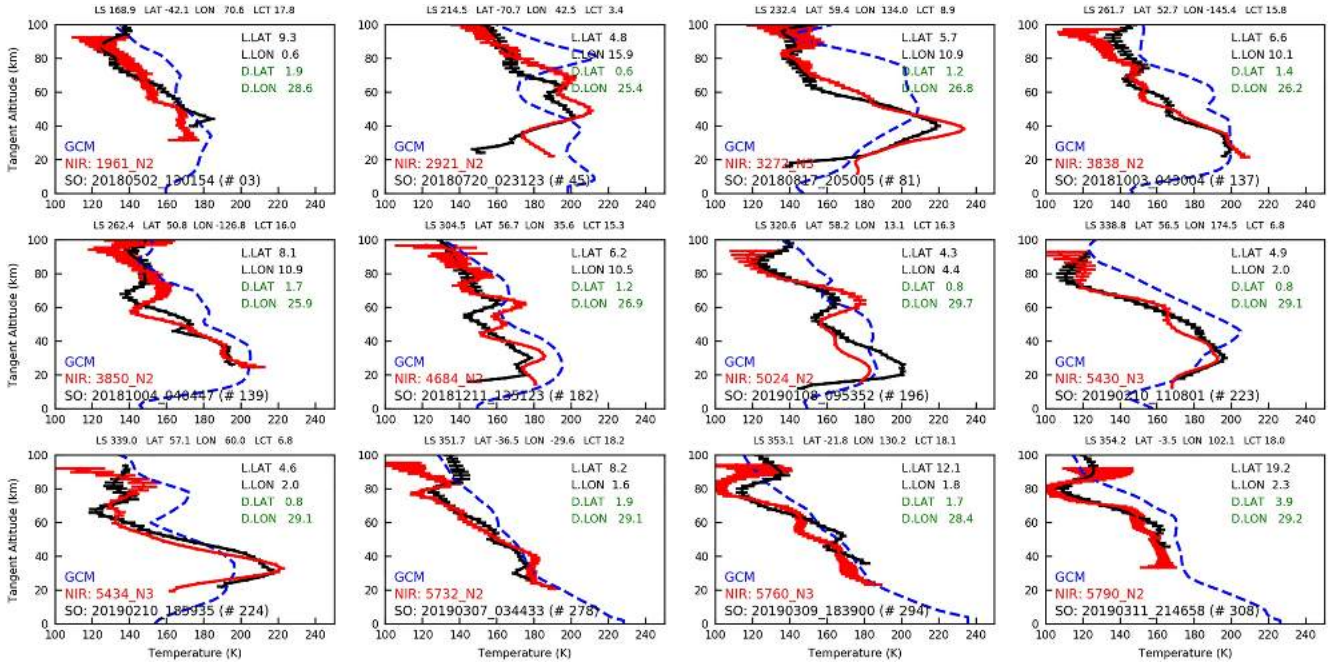

Figure 16. Similar to Figure 15 but for a selection of 12 NOMAD/SO and ACS/NIR profiles which show a good agreement between them and significant differences with the global climate models a priori profile. See text for details.

The number of coincidences between NOMAD/SO and ACS/NIR increases significantly when the criterion for geographical collocation is relaxed. In particular, with a relaxation in longitude to $\Delta LON < 30°$ we allow for profiles from adjacent orbits and then we found 95 coincidences. All these, which include the previous 6 closest ones, are shown in Appendix A, using a similar format to Figure 15. In general, considering the different retrieval methods and instrument characteristics, and the likely effect of a 30° shift in longitude, we consider the agreement as satisfactory. We observed many good matches, but also some significant discrepancies; we show examples of these two subsets in Figures 16 and 17.

Figure 16 shows a dozen of profiles with a good agreement between NOMAD/SO and ACS/NIR and which also present significant deviations from the a priori. The agreement is good except at the very top altitudes and at the bottom of the profiles, where noise and aerosols limit the sounding, respectively. Considering the different retrieval methods, instrument performances and spectral ranges used in our work and in Fedorova et al. (2020), these 12 profiles can be considered as robust determinations of the atmospheric state, and may be particularly valuable for GCM validation purposes. The largest discrepancies are found at mesospheric altitudes, and they present much colder temperatures than in the GCM, but also in some profiles there are discrepancies with the a priori below 50 km, like NOMAD/SO profiles #45, 81, 182, and 224 (see numbers in bracket in Figure 16). It would be interesting to extend the retrievals of both instruments to a couple of Mars years, in search for more significant deviations from the GCM climatological predictions.

Figure 17 shows a selection of another dozen profiles but in this case with clear differences between NOMAD/SO and ACS/NIR. As in the case of Figure 16, the separation between the "coincident" profiles is about 30°, which as said above, may play a role and partly explain some of the differences. The discrepancies are particularly large at mesospheric altitudes, and in general the NOMAD/SO profiles seem to be colder than the ACS/NIR at those altitudes. Again, it will be useful to explore more differences with ACS/NIR in the future, when both instruments' retrieval schemes are applied to a more extended data set including a couple of full Martian years.

5. Conclusions

We present in this work the results of vertical profiles of temperature and CO_2 density from SO observations by the NOMAD/SO channel in its diffraction order 149 during the first year of TGO science operations.

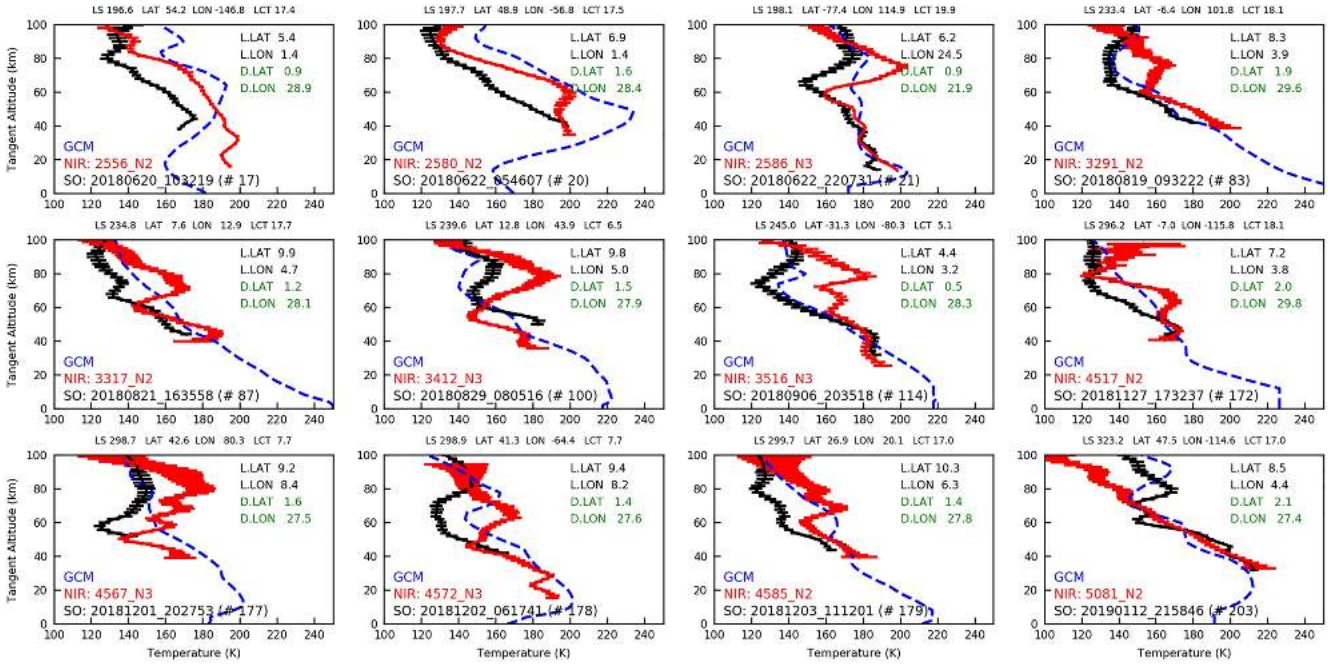

Figure 17. Similar to Figure 15 but for the 12 NOMAD/SO and ACS/NIR profiles with the largest differences. See text for details.

For this purpose we adapted a well tested inversion scheme on Earth limb sounding experiments to SO data on Mars for the first time. This scheme is used in a sequential manner to retrieve diverse targets from the NOMAD/SO data. Results on aerosol opacity's and physical properties, and on H_2O and CO abundance profiles are presented in companion papers in this special issue. The analysis starts with a pre-processing phase, which permits to clear the SO calibrated transmittance of remaining issues like spectral shifts and bendings. This is followed by the actual retrieval, following an iterative application of a precise forward model, which uses micro-windows to eliminate severe contamination from adjacent diffraction orders, and solves temperature and density consistently, with incorporation of hydrostatic adjustments in each iteration. The inversion achieves best-fits with a high degree of convergence in the data set analyzed here. The scheme is robust against a priori assumptions and permits meaningful retrievals typically up to about 90 km altitude.

The atmospheric thermal structure during the two Mars seasons in MY34 (the Martian perihelion half-year period) is characterized by the strong MY34 GDS episode, a well documented event peaking around Ls 195°–210° (Guzewich et al., 2019; Montabone et al., 2020). Our results show that the GDS warmed the atmosphere significantly at all sounded altitudes, with episodes where 180 K are observed at 80 km altitude in the NH and up to 100 km in the SH. The thermal impact is clearly observed during an extended decay phase up to about Ls 250°. During this period the retrievals are difficult in the troposphere due to the strong dust opacity. The impact of the regional dust storm (RDS) around Ls 330°, near the end of the period studied in this work, is less clear in our data. This can be due to several reasons. The first one is the lower amount of aerosols injected into the atmosphere by the regional storm. A second possible reason is the limited sampling in space and time that solar occultations have from the TGO orbit; this mapping may have skipped the peak activity of this RDS.

Regarding the comparison of the retrieved thermal structure with the LMD Mars GCM simulations used here as a priori, the NOMAD temperatures are in good agreement at tropospheric altitudes but are generally wavier and colder at mesospheric altitudes. The atmospheric oscillations reach values close to the CO_2 condensation temperature at mesospheric altitudes much more frequently than in the GCM. This may be explained by a stronger atmospheric tidal activity than in the model, particularly during the GDS peak and decay phases, but also elsewhere through the perihelion season. In particular, a warm layer around 80 km is found in the morning terminator in the NH during Ls 260°–300°, which is clearly absent in the GCM. A warm layer is also observed in the evening terminator but more sporadically. These two global results, a colder mesosphere and a warm layer around 80 km were also found very recently by Belyaev et al. (2021).

Regarding the latitudinal and local time variations, our data is patchy and the TGO orbital mapping does not allow us to build pure latitude or pure local time cross sections. Instead, some boxing is required, which are not free from a mixture of effects. However, with the help of scan-to-scan comparisons with the GCM and of global maps created with the GCM specifically for this comparisons, it seems that our NOMAD retrievals do track the expected thermal structure typical of equinoxes and solstices during the observed period. The main conclusions regarding local time variations is the clearly stronger tidal activity in the morning terminator, mentioned above.

A second retrieval product is the atmospheric CO_2 density, whose global distribution shows very clear latitudinal effects, especially when looking at a single altitude, like 70 km. On top of these, a seasonal trend seems also present, although the occurrence of the GDS in the early Southern Spring dominates the seasonal pattern and hides the expected maximum around Ls 270° that should be typical of non-GDS Mars years. It will be very interesting to revisit this when an extended SO data set covering several MY are processed.

Another interesting product of our retrieval scheme is the so called "LOS correction," which permits to revisit the hydrostatic assumption, based on using a given pressure level at a given altitude, usually taken from the climatology or a priori data set. In our case, the correction indicates that the LMD MGCM pressures at the lowermost tangent altitude of our retrieval range are globally correct, except for a small correction of a couple of km. This agreement is better in dust-clear conditions, when our sounding can be extended to the lower troposphere, below 20 km. Below this altitude, the lower the sounding, the smaller the correction. In some scans the altitude adjustment to reconcile NOMAD and GCM can reach up to 10 km.

We plan to continue the analysis of NOMAD/SO data by extending our retrieval scheme to the whole SO data set available to date, covering two full Mars Years. A few issues remain to be improved also and we plan to tackle them, in a joint effort with other NOMAD teams. These include a better characterization of the SO measurement noise in order to eliminate remaining systematics, and the combination of two different SO orders. For example, the combination of orders 149 and 165, this one with much stronger absorption lines from the CO_2 2.7-μm fundamental band, should help to extend the retrieval range from 90 km up to 160 or 170 km. In addition, the application of our retrieval scheme to the ACS/MIR data is an ongoing task in our team at IAA/CSIC. The results and comparisons between NOMAD/SO and ACS/MIR during a full Mars year will be presented elsewhere.

Appendix A: Sample of 95 Near Coincidences Between NOMAD/SO and ACS/NIR

As explained in Section 4.9, we performed a comparison of our NOMAD/SO temperature retrievals with the ACS/NIR thermal profiles reported by Fedorova et al. (2020), which approximately extend over the last half of MY34. A total of 95 "near coincidences" are found when using the following selecting criteria in solar longitude, latitude, longitude and local time: $\Delta L < 0.1°$, $\Delta LAT < 5°$, $\Delta LON < 30°$ and $\Delta LCT = 0.5$ hr. The 95 comparisons are shown in Figures A1 to A8, split in 8 subsets of a dozen profiles each. Notice that these figures contain the comparisons already shown in Figures 15–17 above.

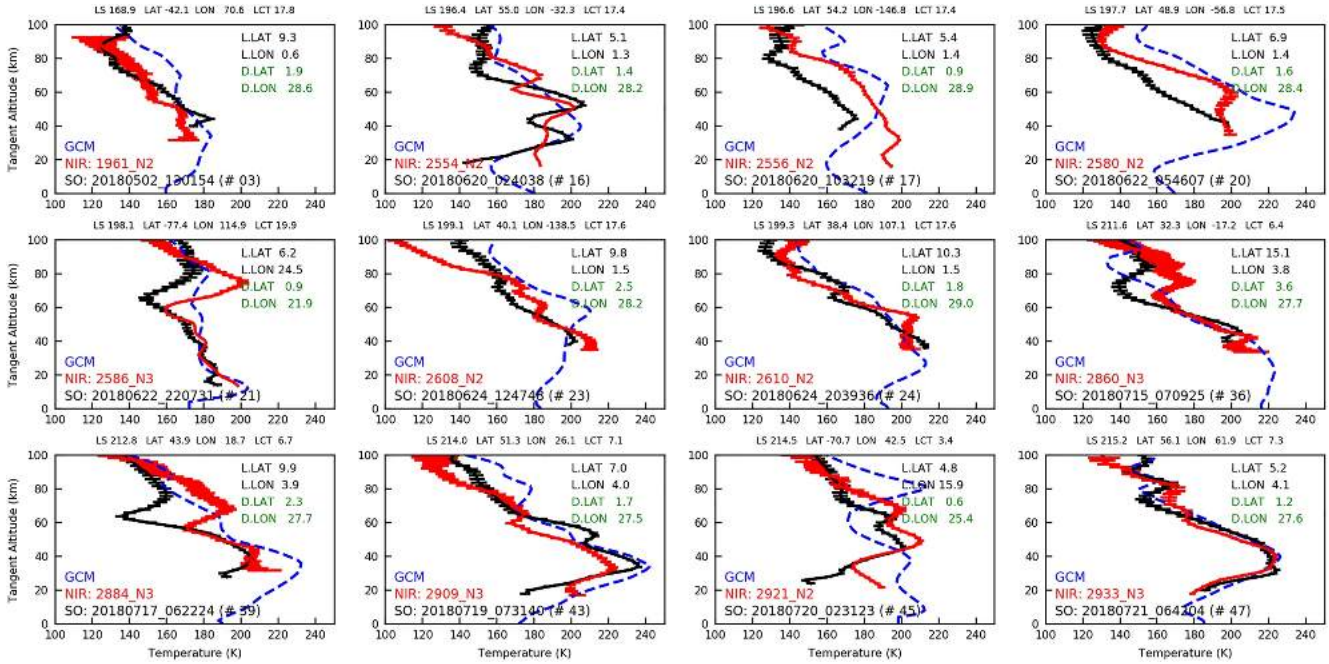

Figure A1. First dozen of NOAMD/SO and ACS/NIR collocated profiles from the set of 95 coincidences mentioned in the text. Figure format similar to Figure 15.

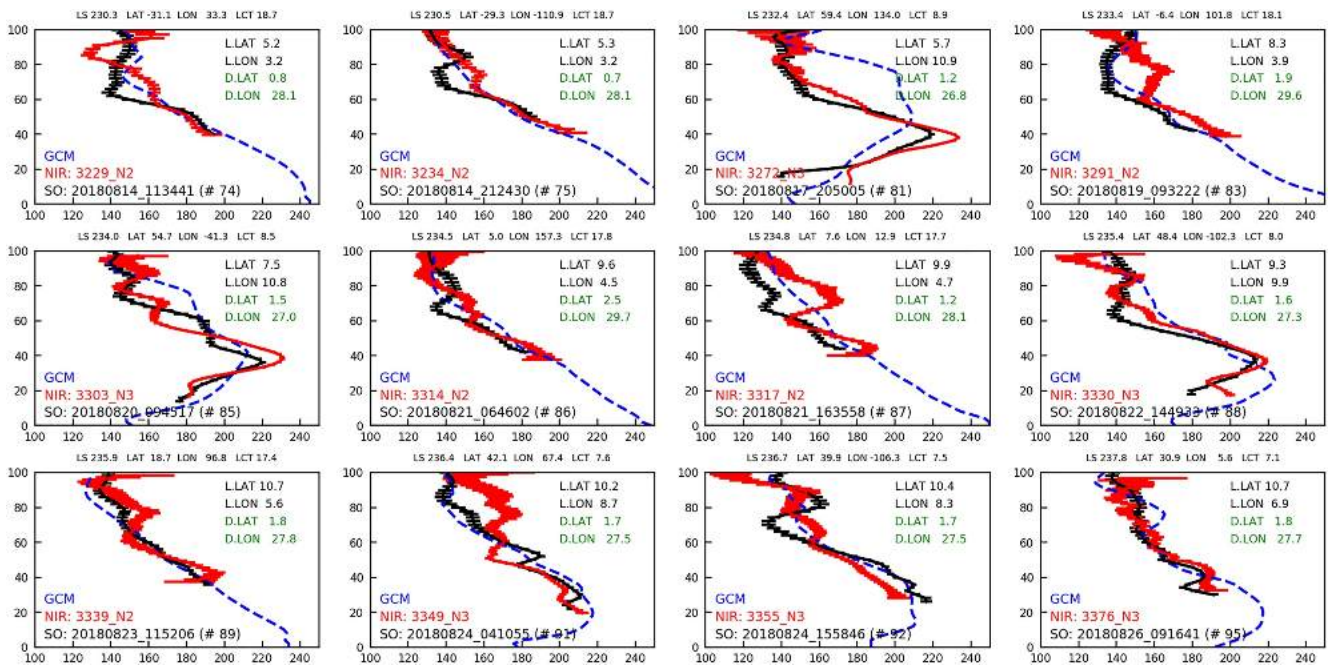

Figure A2. As Figure A1 but for the second dozen of profiles.

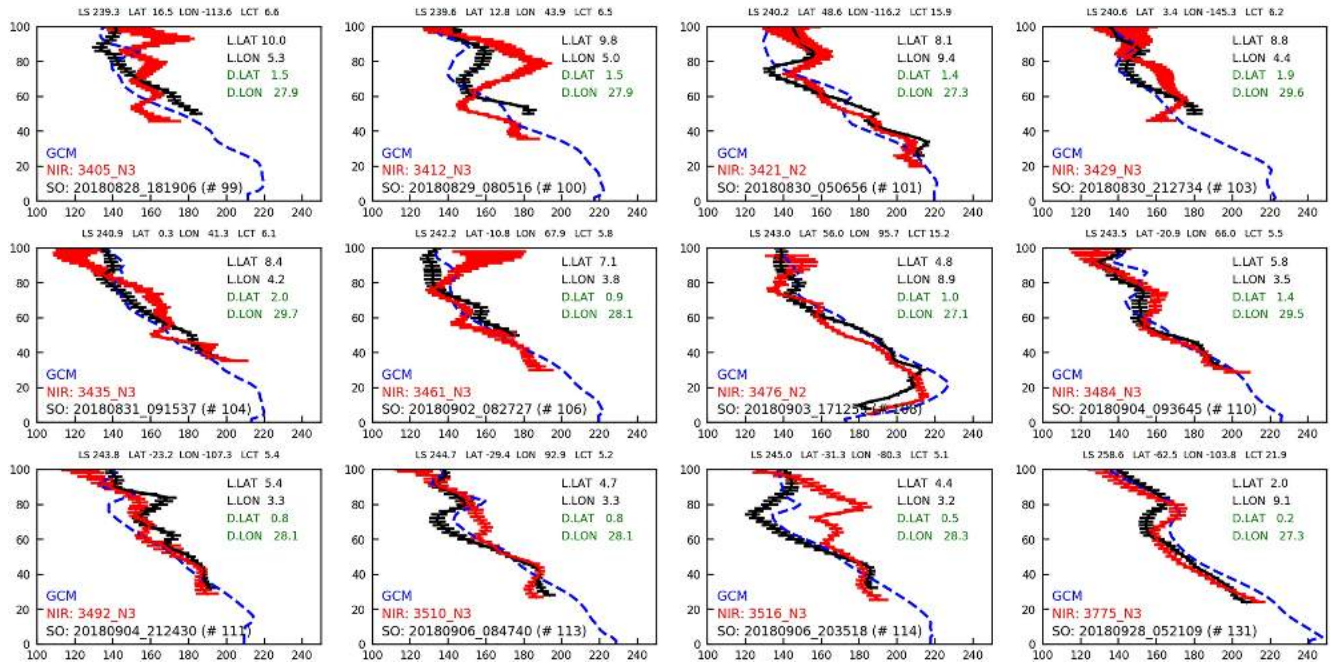

Figure A3. As Figure A1 but for the third dozen of profiles.

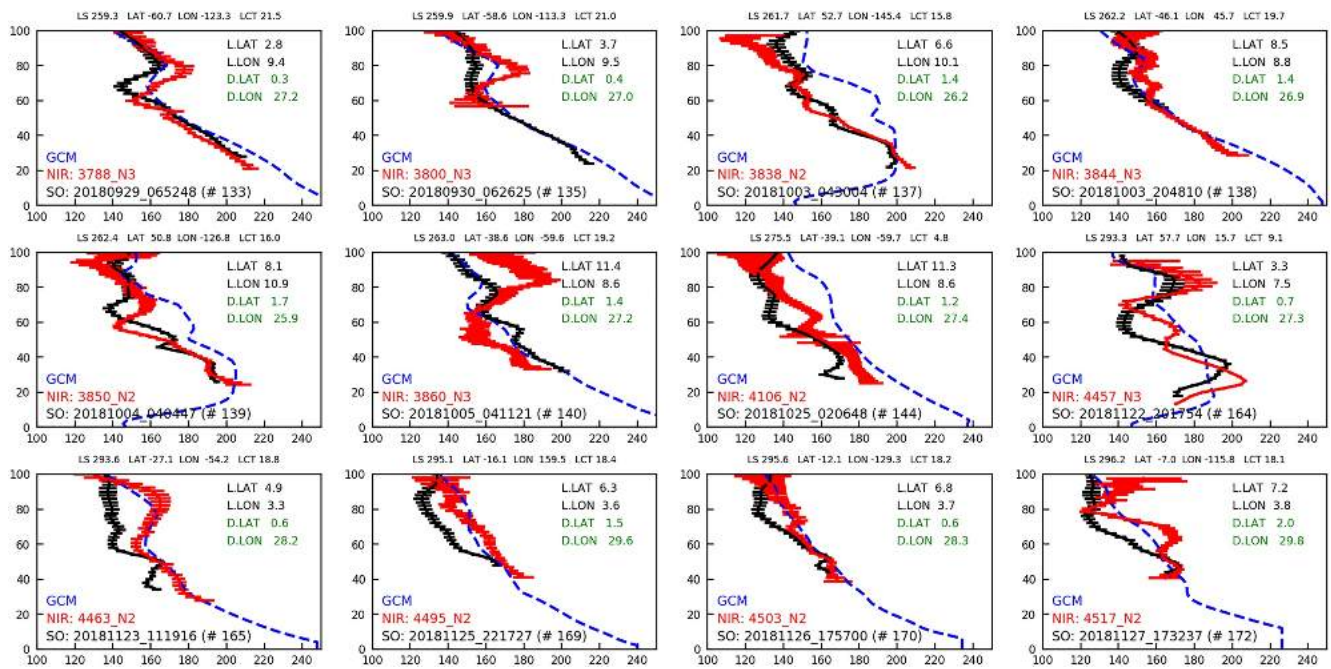

Figure A4. As Figure A1 but for the fourth dozen of profiles.

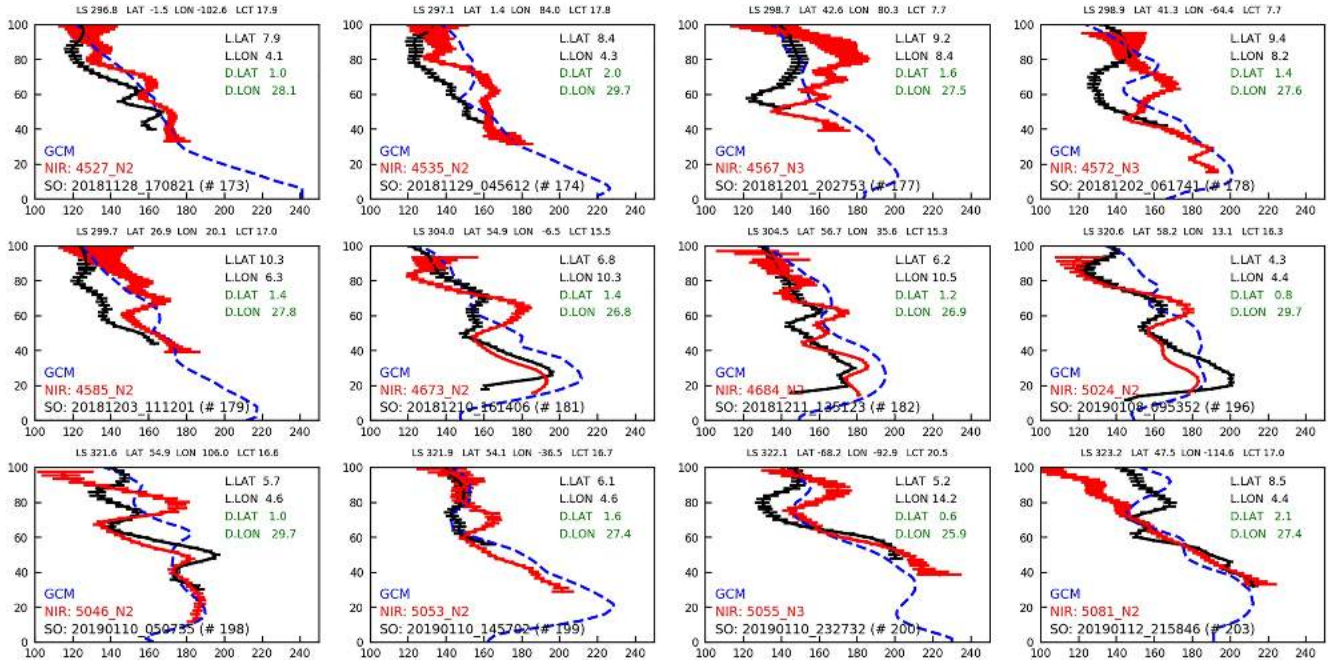

Figure A5. As Figure A1 but for the fifth dozen of profiles.

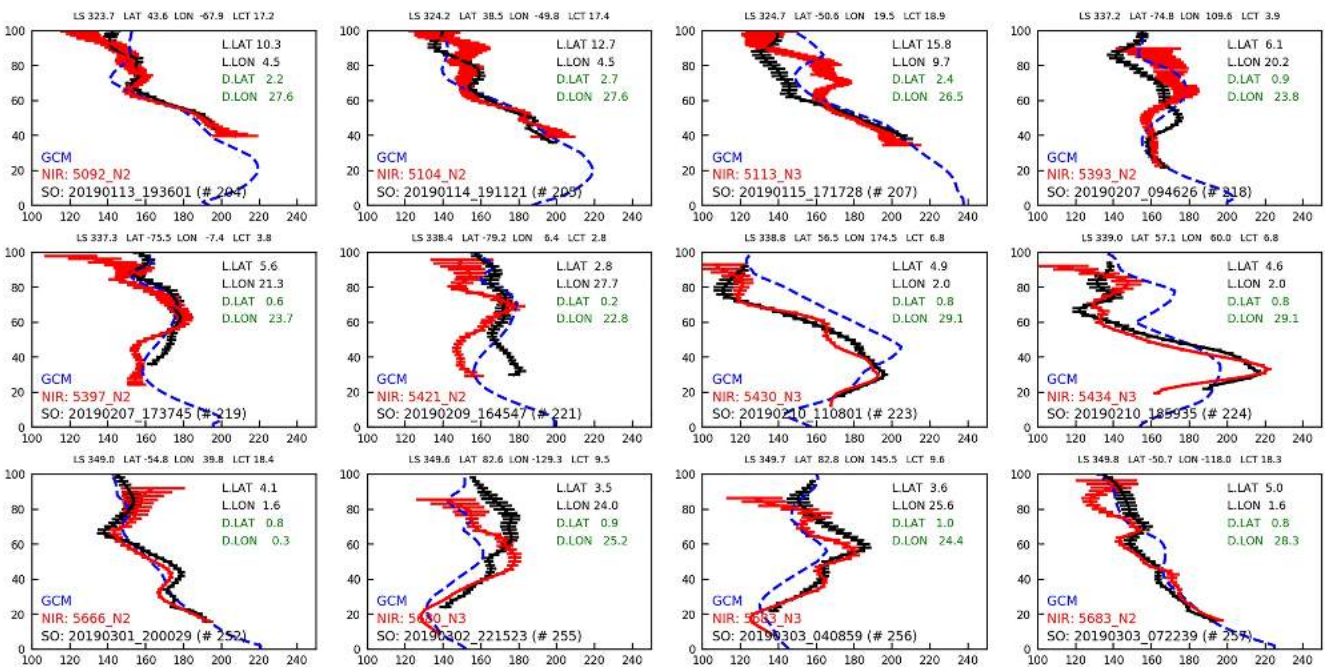

Figure A6. As Figure A1 but for the sixth dozen of profiles.

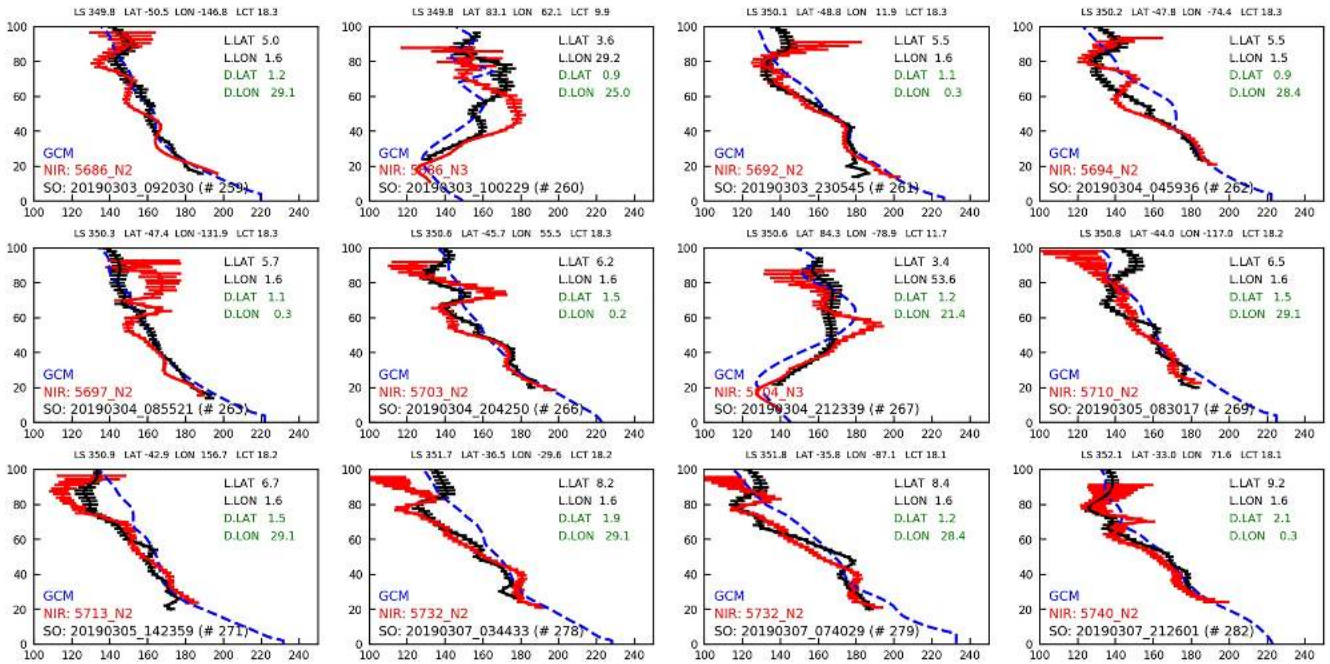

Figure A7. As Figure A1 but for the seventh dozen of profiles.

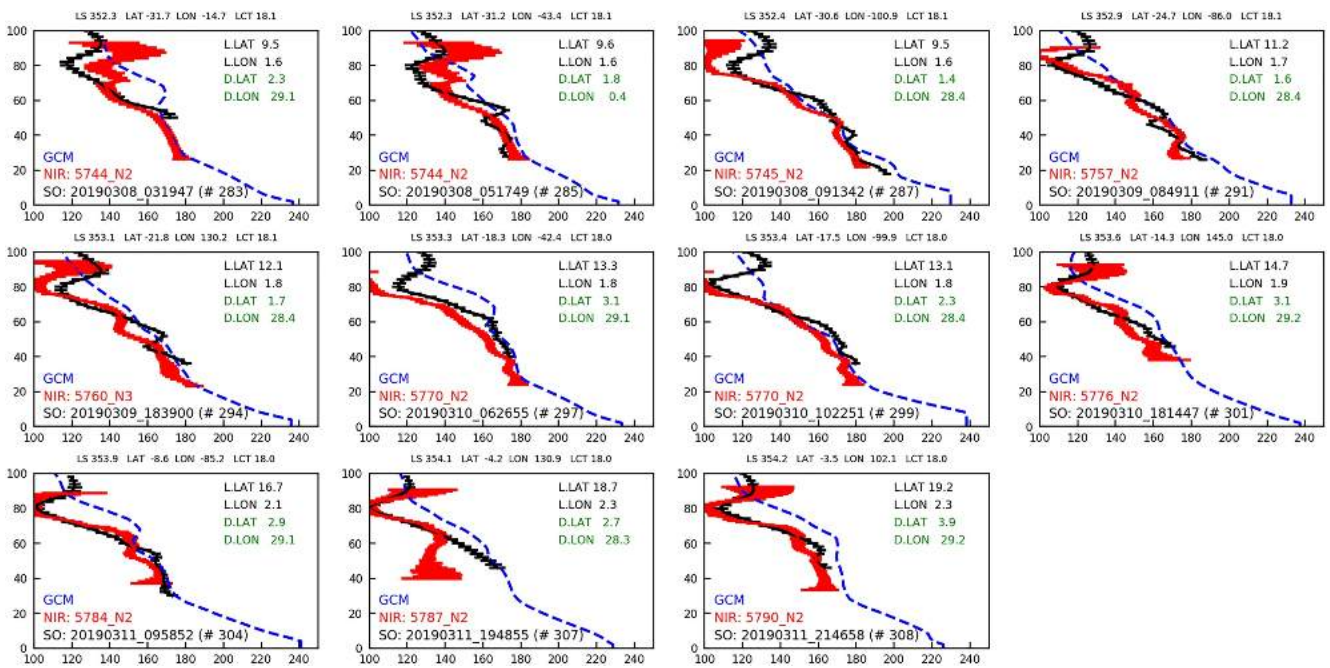

Figure A8. As Figure A1 but faor the eighth dozen of profiles.

Data Availability Statement

The NOMAD-SO Level 1a calibrated transmittance data used in this work are available at the European Space Agency (ESA) planetary archive (https://archives.esac.esa.int/psa), and also at the NOMAD data center (https://nomad.aeronomie.be/index.php/data (Thomas et al., 2021), (Vandaele et al., 2019)). The results retrieved from the NOMAD measurements presented in this article are being archived and available from López-Valverde (2022).

Acknowledgments
The IAA/CSIC team acknowledges financial support from the State Agency for Research of the Spanish MCI through the 'Center of Excellence Severe Ochoa' award for the Instituto de Astrofísica de Andalucia (DEV-2017-0709) and funding by grants PGC2018-101836-B-100 (MCI/AEI/FEDER, EU), PID2019-110689RB-I00/AEI/10.13039/501100011033, and RTI2018-100920-J-I00. ExoMars is a space mission of the European Space Agency (ESA) and Roscosmos. The NOMAD experiment is led by the Royal Belgian Institute for Space Aeronomy (IASB-BIRA), assisted by Co-PI teams from Spain (IAA-CSIC), Italy (INAF-IAPS), and the United Kingdom (Open University). This project acknowledges funding by the Belgian Science Policy Office (BELLS), with the financial and contractual coordination by the ESAU Prod ex Office (PEA 4000103401, 4000121493) as well as by UK Space Agency through Grant ST/V002295/1, ST/V005332/1 and ST/S00145X/1 and Italian Space Agency through Grant 2018-2-HHS.0. US investigators were supported by the National Aeronautics and Space Administration. This work was supported by the Belgian Funds de la Recherche Scientific—FIRS under Grant 30442502 (ET_HOME). This project has received funding from the European Union Horizon 2020 research and innovation program under grant agreement No 101004052 (Road Map project). We want to thank the LMD and LATMOS teams for the continuous development of the LMD-MGCM.

References

Belyaev, D. A., Fedorova, A. A., Trokhimovskiy, A., Alday, J., Montmessin, F., Korablev, O. I., et al. (2021). Revealing a high water abundance in the upper mesosphere of Mars with ACS onboard TGO. *Geophysical Research Letters*, *48*(10), e2021GL093411. https://doi.org/10.1029/2021GL093411

Brines, A., López-Valverde, M. A., Stolzenbach, A., Modak, A., Funke, B., Galindo, F. G., et al. (2023). Water vapor vertical distribution on Mars during perihelion season of MY 34 and MY 35 with ExoMars-TGO/NOMAD observations. *Journal of Geophysical Research: Planets*, *128*, e2022JE007273. https://doi.org/10.1029/2022JE007273

Fedorova, A. A., Montmessin, F., Korablev, O., Luginin, M., Trokhimovskiy, A., Belyaev, D. A., et al. (2020). Stormy water on Mars: The distribution and saturation of atmospheric water during the dusty season. *Science*, *367*(6475), 297–300. https://doi.org/10.1126/science.aay9522

Forget, F., Hourdin, F., Fournier, R., Hourdin, C., Talagrand, O., Collins, M., et al. (1999). Improved general circulation models of the Martian atmosphere from the surface to above 80 km. *Journal of Geophysical Research*, *104*(E10), 24155–24176. https://doi.org/10.1029/1999je001025

Forget, F., Montmessin, F., Bertaux, J.-L., González-Galindo, F., Lebonnois, S., Quémerais, E., et al. (2009). Density and temperatures of the upper Martian atmosphere measured by stellar occultations with Mars Express SPICAM. *Journal of Geophysical Research*, *114*(E1), E01004. https://doi.org/10.1029/2008JE003086

Guzewich, S. D., Lemmon, M., Smith, C. L., Martinez, G., de Vicente-Retortillo, A., Newman, C. E., et al. (2019). Mars Science Laboratory observations of the 2018/Mars year 34 global dust storm. *Geophysical Research Letters*, *46*(1), 71–79. https://doi.org/10.1029/2018GL080839

Jiménez-Monferrer, S., López-Valverde, M. A., Funke, B., González-Galindo, F., Picciali, A., García-Comas, M., et al. (2021). CO_2 retrievals in the Mars daylight thermosphere from its 4.3 μm limb emission measured by OMEGA/MEx. *Icarus*, *353*, 113830. https://doi.org/10.1016/j.icarus.2020.113830

Korablev, O., Montmessin, F., Trokhimovskiy, A., Fedorova, A.-A., & Shakun, A.-V. (2018). The atmospheric chemistry suite (ACS) of three spectrometers for the EXoMars 2016 trace gas orbiter. *Space Science Reviews*, *214*(1), 62. https://doi.org/10.1007/s11214-017-0437-6

López-Valverde, M. A. (2022). IAA/CSIC temperature and CO_2 density profiles in Mars year 34 retrieved from the 1st year of NOMAD/TGO solar occultation observations [Dataset]. https://doi.org/10.5281/zenodo.7086187

López-Valverde, M. A., Gerard, J.-C., González-Galindo, F., Vandaele, A.-C., Thomas, I., Korablev, O., et al. (2018). Investigations of the Mars upper atmosphere with EXoMars trace gas orbiter. *Space Science Reviews*, *214*(1), 29. https://doi.org/10.1007/s11214-017-0463-4

Mahieux, A., Vandaele, A., Robert, S., Wilquet, V., Drummond, R., Valverde, M. L., et al. (2015). Rotational temperatures of Venus upper atmosphere as measured by SOIR on board Venus Express. *Planetary and Space Science*, *113–114*, 347–358. https://doi.org/10.1016/j.pss.2014.12.020

Modak, A., López-Valverde, M. A., Brines, A., Stolzenbach, A., Funke, B., González-Galindo, F., et al. (2023). Retrieval of Martian atmospheric CO vertical profiles from NOMAD observations during the first year of TGO operations. *Journal of Geophysical Research: Planets*, *128*, e2022JE007282. https://doi.org/10.1029/2022JE007282

Montabone, L., Forget, F., Millour, E., Wilson, R., Lewis, S., Cantor, B., et al. (2015). Eight-year climatology of dust optical depth on Mars. *Icarus*, *251*, 65–95. https://doi.org/10.1016/j.icarus.2014.12.034

Montabone, L., Spiga, A., Kass, D. M., Kleinboehl, A., Forget, F., & Millour, E. (2020). Martian year 34 column dust climatology from Mars climate sounder observations: Reconstructed maps and model simulations. *Journal of Geophysical Research: Planets*, *125*(8), e2019JE006111. https://doi.org/10.1029/2019JE006111

Nakagawa, H., Jain, S. K., Schneider, N. M., Montmessin, F., Yelle, R. V., Jiang, F., et al. (2020). A warm layer in the nightside mesosphere of Mars. *Geophysical Research Letters*, *47*(4), e2019GL085646. https://doi.org/10.1029/2019GL085646

Navarro, T., Forget, F., Millour, E., & Greybush, S. J. (2014). Detection of detached dust layers in the martian atmosphere from their thermal signature using assimilation. *Geophysical Research Letters*, *41*(19), 6620–6626. https://doi.org/10.1002/2014GL061377

Neefs, E., Vandaele, A. C., Drummond, R., Thomas, I. R., Berkenbosch, S., Clairquin, R., et al. (2015). NOMAD spectrometer on the EXoMars trace gas orbiter mission: Part 1—Design, manufacturing and testing of the infrared channels. *Applied Optics*, *54*(28), 8494–8520. https://doi.org/10.1364/AO.54.008494

Robert, S., Vandaele, A., Thomas, I., Willame, Y., Daerden, F., Delanoye, S., et al. (2016). Expected performances of the NOMAD/EXoMars instrument. *Planetary and Space Science*, *124*, 94–104. https://doi.org/10.1016/j.pss.2016.03.003

Rodgers, C. D. (2000). *Inverse methods for atmospheric sounding - theory and practice, Series on Atmospheric Oceanic and Planetary Physics* (Vol. 2). World Scientific Publishing Co. Pte. Ltd. https://doi.org/10.1142/3171

Smith, M. D., Bougher, S. W., Encrenaz, T., Forget, F., & Kleinböhl, A. (2017). Thermal structure and composition. In R. M. Haberle, R. T. Clancy, F. Forget, M. D. Smith, & R. W. Zurek (Eds.), *The atmosphere and climate of Mars* (pp. 42–75). Cambridge University Press. https://doi.org/10.1017/9781139060172.004

Starichenko, E. D., Belyaev, D. A., Medvedev, A. S., Fedorova, A. A., Korablev, O. I., Trokhimovskiy, A., et al. (2021). Gravity wave activity in the martian atmosphere at altitudes 20–160 km from ACS/TGO occultation measurements. *Journal of Geophysical Research: Planets*, *126*(8), e2021JE006899. https://doi.org/10.1029/2021JE006899

Stiller, G. P. (2000). The Karlsruhe optimized and precise radiative transfer Algorithm (KOPRA) (Vol. FZKA 6487). Forschungszentrum Karlsruhe.

Thomas, I. R., Aoki, S., Trompet, L., Robert, S., Depiesse, C., Willame, Y., et al. (2021). Calibration of NOMAD on ESA's EXoMars trace gas orbiter: Part 1? The solar occultation channel. *Planetary and Space Science*, *218*, 105411. https://doi.org/10.1016/j.pss.2021.105411

Thomas, I. R., Vandaele, A. C., Robert, S., Neefs, E., Drummond, R., Daerden, F., et al. (2016). Optical and radiometric models of the NOMAD instrument part II: The infrared channels—SO and LNO. *Optics Express*, *24*(4), 3790–3805. https://doi.org/10.1364/OE.24.003790

Trompet, L., Mahieux, A., Ristic, B., Robert, S., Wilquet, V., Thomas, I. R., et al. (2016). Improved algorithm for the transmittance estimation of spectra obtained with SOIR/Venus express. *Applied Optics*, *55*(32), 9275–9281. https://doi.org/10.1364/AO.55.009275

Trompet, L., Vandaele, A. C., Thomas, I., Aoki, S., Daerden, F., Erwin, J., et al. (2023). Carbon dioxide retrievals from NOMAD-SO on ESA's ExoMars Trace Gas Orbiter and temperature profiles retrievals with the hydrostatic equilibrium equation: 1. Description of the method. *Journal of Geophysical Research: Planets*, *128*, e2022JE007277. https://doi.org/10.1029/2022JE007277

Vandaele, A. C., Korablev, O., Daerden, F., Aoki, S., Thomas, I. R., Altieri, F., et al. (2019). Martian dust storm impact on atmospheric H_2O and D/H observed by EXoMars trace gas orbiter. *Nature*, *568*(7753), 521–525. https://doi.org/10.1038/s41586-019-1097-3

Vandaele, A. C., Lopez-Moreno, J.-J., Patel, M. R., Bellucci, G., Daerden, F., Ristic, B., et al. (2018). NOMAD, an integrated suite of three spectrometers for the EXoMars trace gas mission: Technical description, science objectives and expected performance. *Space Science Reviews*, *214*(5), 80. https://doi.org/10.1007/s11214-018-0517-2

Villanueva, G. L., Liuzzi, G., Aoki, S., Stone, S. W., Brines, A., Thomas, I. R., et al. (2022). The deuterium isotopic ratio of water released from the martian caps as measured with TGO/NOMAD. *Geophysical Research Letters*, *49*(12), e2022GL098161. https://doi.org/10.1029/2022GL098161

Villanueva, G. L., Mumma, M. J., Smith, M. D., Daerden, F., & Ristic, B. (2018). Methane on Mars: New insights into the sensitivity of CH_4 with the NOMAD/EXoMars spectrometer through its first in-flight calibration. *Icarus*, *321*, 671–690. https://doi.org/10.1016/j.icarus.2018.09.021

von Clarmann, T., Glatthor, N., Grabowski, U., Höpfner, M., Kellmann, S., Kiefer, M., et al. (2003). Retrieval of temperature and tangent altitude pointing from limb emission spectra recorded from space by the Michelson Interferometer for Passive Atmospheric Sounding (MIPAS). *Journal of Geophysical Research*, *108*(D23), 4736. https://doi.org/10.1029/2003JD003602

Wolff, M., López-Valverde, M. A., Madeleine, J.-B., John Wilson, R., Smith, M. D., Foucher, T., & Delory, G. T. (2017). Chapter 6—Radiative processes: Techniques and applications. In B. Haberle, M. Smith, T. Clancy, F. Forget, & R. Zurek (Eds.), *The atmosphere and climate of Mars* (pp. 106–171). Cambridge University Press. https://doi.org/10.1017/9781139060172